Revisiting Disc-Jet Coupling in Black Hole X-ray Binaries: On the Nature of Disc Dynamics and Jet Velocity

Sreetama Das Choudhury[1]⋆, Bhuvana G. R.[2]†, Santabrata Das[1]‡ and Anuj Nandi[3]§
[1]Department of Physics, Indian Institute of Technology Guwahati, Guwahati, 781039, India.
[2]Institute for Advanced Study, Gifu University, 1-1 Yanagido, Gifu 501-1193, Japan.
[3]Space Astronomy Group, ISITE Campus, U. R. Rao Satellite Center, Outer Ring Road, Marathahalli, Bengaluru, 560037, India.

Accepted XXX. Received YYY; in original form ZZZ

ABSTRACT

We perform a comprehensive wide-band ($3-100$ keV) spectro-temporal analysis of thirteen outbursting black hole X-ray binaries (BH-XRBs), utilizing data (quasi)simultaneous with radio observations to unravel the complex disc-jet connection. *RXTE* observations are analyzed for XTE J1859 + 226, GX 339 − 4 (2002, 2006, and 2010 outbursts), 4U 1543 − 47, H1743 − 322 (2003 and 2009 outbursts), XTE J1550 − 564, XTE J1752 − 223, XTE J1650 − 500, Swift J1753.5 − 0127, XTE J1748 − 288, and GRO J1655 − 40. For Swift J1727.8 − 1613 and MAXI J1535 − 571, we utilize *HXMT* data, while both *AstroSat* and *HXMT* observations are analyzed for Swift J1658.2 − 4242. Type-C QPOs observed in harder states (LHS, HIMS; $F_{nth} \geq 0.4$) exhibit positive lag for low-inclination sources ($i < 50^\circ$), whereas it generally exhibits negative lag for high-inclination sources ($i > 60^\circ$), except XTE J1550 − 564, Swift J1727.8 − 1613, H1743 − 322 (2003 outburst) and GRO J1655 − 40. Notably, type-A QPOs exhibit negative lags ($\sim 1-10$ ms) regardless of source inclination, while type-B QPOs show positive lags in low-inclination sources, and both positive and negative lags ($\sim 1-15$ ms) in high-inclination sources, typically occurring in SIMS ($F_{nth} \lesssim 0.45$). Systematic appearance of type-A QPOs preceding radio flares in several sources suggests that type-A QPOs indicate telltale signs of jet ejection, while type-B QPOs are closely linked with radio flares (*i.e.*, transient jets). Present findings suggest the corona evolves from a radially extended to a vertically elongated structure during the type-C to type-B transition via type-A QPOs, with type-B QPOs linked to radially compact or vertically extended coronal geometries, resembling jet ejection. The strong radio–X-ray luminosity correlation seems to provide compelling evidence of accretion-powered jets. Finally, we find that jets in SIMS are moderately relativistic in nature with velocities $\gtrsim 0.3-0.8\,c$ in BH-XRBs under consideration.

Key words: accretion, accretion disc – black hole physics – X-rays: binaries – stars: individual– stars: jets

1 INTRODUCTION

Galactic black hole X-ray binaries (BH-XRBs) are considered as the ideal cosmic laboratories to understand the accretion-ejections mechanism (Mirabel & Rodríguez 1994; Fender et al. 2004, 2009; Belloni et al. 2011; Miller-Jones et al. 2012; Radhika & Nandi 2014; Radhika et al. 2016; Bright et al. 2020; Espinasse et al. 2020; Nandi et al. 2024, and references therein). Indeed, the imprint of disc-jet connections are encoded in the spectro-temporal features of the outbursting BH-XRBs. During an outbursting phase, BH-XRBs exhibit outflow activities in the form of jets, which after being ejected, expands adiabatically and emits synchrotron radiations in infrared and radio. A correlation between X-ray and radio lightcurves is observed in many BH-XRBs (Mirabel et al. 1998), where the radio emission is observed after a delay (Mirabel et al. 1998; Corbel et al. 2005; Russell et al. 2019; Homan et al. 2020; Espinasse et al. 2020; Monageng et al. 2021) with respect to X-ray emission. Hence, these cosmic entities offer an excellent opportunity for exploring the accretion-ejection processes in strong gravity environment around black holes.

BH-XRBs are categorized either as persistent (Chen et al. 1997; Remillard & McClintock 2006; Tetarenko et al. 2016; Corral-Santana et al. 2016) or transient (Tanaka & Shibazaki 1996; Remillard & McClintock 2006; Sreehari et al. 2018) based on their overall characteristics and therefore, these sources are expected to undergo evolution driven by their accretion dynamics. It is worth mentioning that the evolution of accretion discs of outbursting BH-XRBs are studied through the Hardness Intensity Diagram (HID) (also referred as Q-diagram; Maccarone & Coppi 2003; Belloni 2004; Homan & Belloni 2005; Belloni et al. 2005; Remillard & McClintock

⋆ E-mail: d.sreetama@iitg.ac.in
† E-mail: bhuvanahebbar@gmail.com
‡ E-mail: sbdas@iitg.ac.in
§ E-mail: anuj@ursc.gov.in

2006; Motta et al. 2009; Nandi et al. 2012; Aneesha et al. 2019; Sreehari & Nandi 2021; Nandi et al. 2024), which typically traces out all four spectral states, namely Low Hard State (LHS), Hard Intermediate State (HIMS), Soft Intermediate State (SIMS) and High Soft State (HSS) (Homan et al. 2001; Fender et al. 2004; Belloni et al. 2005; Nandi et al. 2012; Radhika & Nandi 2014; Sreehari et al. 2018; Nandi et al. 2018; Baby et al. 2020; Nandi et al. 2024). Interestingly, different spectral states are associated with the various types of QPOs, which are generally classified into three categories, such as type-C, type-B, and type-A (Wijnands et al. 1999; Homan et al. 2001; Remillard et al. 2002; Homan & Belloni 2005; Ingram et al. 2009; Nandi et al. 2012; Radhika et al. 2018, and references therein). Type-C QPOs are characterized by frequencies $\nu_{\rm QPO} \sim 0.1 - 30$ Hz, quality factor Q ~ 10 and rms amplitudes $\rm rms_{QPO}\% \sim 5 - 20$, and are observed during LHS, HIMS, and sometimes in SIMS (Casella et al. 2004). Their power density spectra (PDS) typically show flat-top noise at low frequencies, followed by red noise at higher frequencies, often accompanied by sub-harmonics and harmonics. Type-B QPOs are observed with $\nu_{\rm QPO} \sim 1 - 7$ Hz (see also Gao et al. 2014), Q $\sim 3 - 6$ and $\rm rms_{QPO}\% \sim 3 - 5$. Their PDS is dominated by red noise and may occasionally show harmonics features. On contrary, type-A QPOs are weak and broad with $\nu_{\rm QPO} \sim 5 - 8$ Hz, Q ≤ 3, and $\rm rms_{QPO}\% \leq 4$. Their PDS is dominated by red noise without any detection of harmonics. Type-A and Type-B QPOs are typically observed during the SIMS. What is more is that Casella et al. (2004, 2005) introduced additional QPO classifications, such as type-C* and type-B cathedral QPOs, which are later reported by Rodriguez & Varnière (2011) and Radhika & Nandi (2014).

Usually, LHS and HIMS exhibit type-C QPOs along with compact radio emission characterized by the flat or inverted spectrum. In these spectral states, the X-ray energy spectra are mostly dominated by the Comptonized high energy radiations over the thermal disc emission, which often best described by the power-law distribution (Chakrabarti & Titarchuk 1995; Zdziarski et al. 1996; Mandal & Chakrabarti 2005; Done et al. 2007; Motta et al. 2009; Iyer et al. 2015; Bhuvana et al. 2023; Aneesha et al. 2024; Banerjee et al. 2024, and references therein). In the outbursting evolutionary track, HIMS is followed by the SIMS, which usually remains softer compared to the HIMS with a relatively stronger dominance of thermal emission. Quite often, SIMS exhibits type-A and type-B QPOs (Belloni et al. 2005; Remillard & McClintock 2006; Fender et al. 2009; Motta et al. 2010; Radhika & Nandi 2014; Gao et al. 2014; Radhika et al. 2016; Homan et al. 2020; Harikrishna & Sriram 2022; Liu et al. 2022; Peirano et al. 2023; Zhang et al. 2023; Ma et al. 2024), and optically thin transient relativistic radio jets are occasionally observed (Fender et al. 2009; McClintock et al. 2009; Miller-Jones et al. 2012; Carotenuto et al. 2021; Wood et al. 2021, 2024). Finally, the source is evolved to HSS with strong thermal emission and relatively weak signature of Comptonized emission, where the jet activity is suppressed completely and QPO signature disappears in the power spectra (Motta et al. 2010; Miller-Jones et al. 2012; Radhika & Nandi 2014; Radhika et al. 2016; Zhang et al. 2023).

Generally, the ejection of jets occurs during the transition from the HIMS to SIMS, as denoted by the jet line in HID (Fender et al. 2004). Moreover, type-B or type-A QPOs are observed concurrent with radio flares, suggesting the occurrence of jet ejection (Fender et al. 2004, 2009; Varnière et al. 2012; Radhika et al. 2016; Homan et al. 2020; Kylafis et al. 2020; Sriram et al. 2021; Harikrishna & Sriram 2022; Zhang et al. 2023). Earlier work of Blandford & Znajek (1977) suggests that the rotational energy of the spinning BH can be extracted and subsequently utilized to power the jets. Indeed, this appealing mechanism indicates that spin of the black hole plays pivotal role in jet activities. Meanwhile, a positive correlation between black hole spin and jet luminosity is observed in several BH-XRBs (Steiner et al. 2012; Narayan & McClintock 2013; McClintock et al. 2014). However, conflicting claims are reported indicating weak correlation between source spin and the observed jet power (Fender et al. 2010; Russell et al. 2013; Aktar et al. 2015, 2017). Interestingly, in spite of having a plethora of X-ray and radio observations, the origin as well as the intrinsic mechanisms responsible for powering the jets still remain inconclusive.

Outbursting BH-XRBs exhibit two types of radio jets, namely compact/steady and transient (Fender et al. 2004). The quiescent state and LHS are characterized by low bulk velocity jets (Lorentz factor $\Gamma \leq 2$) (Fender et al. 1999; Miller-Jones et al. 2012). As X-ray luminosity increases, jet power also increases, showing a non-linear correlation $L_{\rm radio} \propto L_{\rm X}^{0.6-0.7}$ during low hard state (Gallo et al. 2003; Corbel et al. 2003, 2013; Kylafis et al. 2023). With increasing X-ray luminosity, jets in outbursting sources gradually become unstable followed by intense radio emissions indicating the ejection of a faster-moving radio lobe (Fender et al. 2009, and references therein). When colliding with previously ejected jet material, internal shocks are generated, resulting in the production of a bright, optically thin relativistic jets (Miller-Jones et al. 2012). Beside this, an alternative scenario is also suggested, where the excess thermal gradient force across the centrifugally supported shocks diverts a part of the inflowing matter in the form of bipolar jets (Chakrabarti 1999; Das et al. 2001; Kumar & Chattopadhyay 2013; Aktar et al. 2015, 2017; Das et al. 2022; Joshi et al. 2022). These jets are collimated and accelerated by the radiations emanated from the disc (Chattopadhyay 2005). This conjecture is supported by the reduction in hard flux component during SIMS, suggesting the evacuation of corona in launching the bipolar jets (Vadawale et al. 2001; Nandi et al. 2001; Radhika & Nandi 2014; Nandi et al. 2018). Indeed, optically thick jets in hard states appear continuous, steady, and mildly relativistic ($\beta \sim 0.1$) (Dhawan et al. 2000), while optically thin jets in SIMS resolve into plasmoids moving at relativistic speeds ($\beta \sim 0.9$) (Mirabel & Rodríguez 1999). In BH-XRBs, the jet velocity is commonly determined by analyzing resolved images that depict the proper motion of ejected material (Mirabel & Rodríguez 1994; Corbel et al. 2005; Miller-Jones et al. 2012). It is worth mentioning that assessing the relativistic nature of transient jets remains challenging for numerous BH-XRBs due to the non-availability of resolved images of radio ejecta (Fender et al. 2004).

Meanwhile, numerous efforts were made to understand the dynamics of the corona as well as the origin of QPOs through the time/phase lag studies (Reig et al. 2000; Belloni et al. 2005; Dutta & Chakrabarti 2016; van den Eijnden et al. 2017; Zhang et al. 2023). In general, it is argued that positive (hard) lag occurs due to inverse Comptonization of soft photons in the corona (Payne 1980; Miyamoto et al. 1988;

Reig et al. 2000; Dutta & Chakrabarti 2016; Méndez et al. 2022), whereas negative (soft) lag is caused due to Compton down-scattering (Reig et al. 2000), reverberation (Uttley et al. 2014; Karpouzas et al. 2020; Zhang et al. 2023) and gravitational bending (Chatterjee et al. 2017). Meanwhile, Gao et al. (2014) argued that the type-B QPO observed in GX 339 − 4 is associated with the inverse-Comptonization of soft photons in the corona. Similarly, Chatterjee et al. (2020) reported an increase in positive time lag with QPO frequency during the rising phase of the outburst, suggesting that outflows may possibly contribute to positive lags. Muñoz-Darias et al. (2010) observed unusually large time lags ($\sim$ 0.1 s) which appear to be resulted from inverse-Comptonization occurring in the outflows.

Notably, numerous efforts were put forward to examine the origin of type-B QPOs in the realm of vertically extended corona. Belloni et al. (2020) suggested a jet-like corona in MAXI J1348−630 based on observed positive lags, whereas Homan et al. (2020) reported a $\sim$ 2.5 hour delay between type-B QPOs and jet ejection. Stevens & Uttley (2016); Kylafis et al. (2020) proposed the precessing jet base as the hard X-ray source, while Méndez et al. (2022) argued for vertically elongated corona near radio flares in GRS 1915+105. In contrast, Zhang et al. (2023) attributed type-B QPOs involving the precession of an elongated corona, where hard photons fall back to the disc and are reprocessed resulting in negative lags. Furthermore, Liu et al. (2022) argued that type-B QPOs are linked to weaker jets than type-C QPOs.

Previous studies have examined the connections between the type of QPOs, source inclination angles, and time lags for selected BH-XRBs (Dutta & Chakrabarti 2016; van den Eijnden et al. 2017). Incidentally, the role of source inclination in understanding the lag behavior associated with type-A QPOs remains inconclusive. In addition, the connection between the lag characteristics of different QPO types and the jet ejection also remains elusive. Moreover, there has been lack of attempts to estimate jet velocities by correlating radio and X-ray properties during SIMS of BH-XRBs.

Keeping the above considerations in mind, we carry out an in-depth spectro-temporal analysis of X-ray data along with the available radio observations to understand the underlying physical processes active in BH-XRBs. Since jets are believed to originate from the inner accretion disc (Miller-Jones et al. 2012; Méndez et al. 2022; Kylafis et al. 2020), investigating the evolution of the corona characteristics during state transitions provides insight into the disc-jet connection. In this work, we explore the dynamics of the inner accretion disc through wide-band (3 − 100 keV) spectral and timing analyses of thirteen BH-XRBs, namely XTE J1859 + 226, GX 339 − 4 (2002, 2006, and 2010 outbursts), 4U 1543 − 47, H1743 − 322 (2003 and 2009 outbursts), XTE J1550 − 564, XTE J1752 − 223, XTE J1650 − 500, Swift J1753.5 − 0127, XTE J1748 − 288, GRO J1655 − 40, Swift J1727.8 − 1613, MAXI J1535 − 571 and Swift J1658.2 − 4242, using *RXTE*, *HXMT* and *AstroSat* observations. Source selection is done based on the good coverage in radio and X-ray observations, and the wide range of inclination angles ($\sim 35^\circ$ to $\sim 75^\circ$). With this, we investigate the spectro-temporal properties of these sources and using both X-ray and radio observations, we estimate the jet velocities during radio flares. Finally, we attempt to explore the spectro-temporal correlations and examine the role of accretion dynamics in powering jets.

The paper is organized as follows: In Section 2, we briefly describe the data reduction procedure both in X-rays and radio. In Section 3, we discuss the modelling of PDS, time lag calculations, modelling the energy spectra and spin measurement using continuum fitting method. We present our results in Section 4. In Section 5, we estimate the source spin and jet velocity during the radio flares. Finally, we discuss the implications of our results in Section 6 and conclude.

2 OBSERVATION AND DATA REDUCTION

In this work, we examine the inherent disc-jet coupling in several Galactic outbursting BH-XRBs observed with *RXTE*[1], *HXMT*[2] and *AstroSat* (Agrawal 2017). In order to facilitate this, we make use of (quasi-)simultaneous radio observations available as well. We choose sixteen outbursts from thirteen such BH-XRBs, namely XTE J1859+226, H1743−322 (2003 and 2009 outbursts), GX 339 − 4 (2002, 2007 and 2010 outburst), 4U 1543 − 47, XTE J1752 − 223, XTE J1650 − 500, Swift J1753.5 − 0127, XTE J1550 − 564, XTE J1748 − 288, GRO J1655 − 40, Swift J1727.8 − 1613, MAXI J1535 − 571, Swift J1658.2−4242, respectively, which have adequate coverage in X-ray as well as radio. Among them, XTE J1859+226, XTE J1752−223 and Swift J1727.8−1613 showed multiple X-ray and radio peaks in a single outburst during 1999, 2009 and 2023, respectively, whereas remaining sources under considerations exhibited single(multiple) outburst(s) till date.

2.1 X-ray Data

We use thirteen *RXTE* and three *HXMT* and one *AstroSat* archival observations of outbursting BH-XRBs. For XTE J1859+226, the outburst was observed in 1999 − 2000 (Smith 1999) which was continued for 163 days (MJD 51460 to MJD 51626). GX 339−4 exhibited several outbursts. In this study, we focus on the 2002 − 2003 outburst of GX 339−4 (Smith et al. 2002), which lasted for 477 days, using data from MJD 52288.6 to MJD 52765.6 for our analysis. We also consider the 2007 outburst (Soldi et al. 2007), with data spanning from MJD 54102.31 to MJD 54256.58, consisting of 154 days and the 2010 outburst (Yamaoka et al. 2010), covering MJD 55208.48 to MJD 55260.07, comprising of 51 days. For 2002 outburst of 4U 1543−47 (Miller & Remillard 2002), we analyse 73 days (MJD 52442.8 to MJD 52515.5) of pointed observations. For H1743−322, the 2009 outburst (Miller-Jones et al. 2009; Kalemci et al. 2005) persisted for 73 days, spanning from MJD 54980.4 to MJD 55053.8. In addition, we consider the 2003 outburst of H1743−322 (Remillard 2003), specifically selecting observations that are pertinent to time lag analysis and jet velocity estimations. We consider 1998 outburst of XTE J1550−564 (Rutledge et al. 1998) and analyze data for 254 days (MJD 51065 to MJD 51318). For 2009 outburst of XTE J1752−223 (Markwardt et al. 2009), we analyze observations from MJD 55130 to MJD 55414, with a duration of 284 days. In case of XTE J1650−500, we consider the 2002 outburst (Tomsick et al.

[1] https://heasarc.gsfc.nasa.gov/cgi-bin/W3Browse/w3browse.pl
[2] https://archive.hxmt.cn/proposal

2002) from MJD 52158 to MJD 52416 for a duration of 258 days. For Swift J1753.5−0127, we analyze 2005 outburst (Morgan et al. 2005) that lasts for 150 days from MJD 53553 to MJD 53703. For Swift J1727.8−1613, we consider 42 days of observations (MJD 60181 to 60222) from 2023 outburst (Negoro et al. 2023). For XTE J1748–288, we focus on the 1998 outburst (Smith et al. 1998), considering observations spanning from MJD 50968.83 to MJD 51082.14. In the case of GRO J1655–40, we examine the 2005 outburst (Markwardt & Swank 2005), utilizing data recorded between MJD 53421.36 and MJD 53685.20, with 263 days of observations. For MAXI J1535–571, we analyze the 2017 outburst (Negoro et al. 2017), covering the period from MJD 58002.45 to MJD 58177.83, with 18 pointed observations. Finally, for Swift J1658.2–4242, we consider observations from its 2018 outburst (Grebenev et al. 2018), spanning MJD 58169.98 to MJD 58206.77 and consisting of 7 pointed observations by *AstroSat* and 25 pointed observations by *Insight/HXMT*.

We use Binned mode, Event mode and Good Xenon data of *RXTE* for our timing analysis. In order to extract the lightcurves in the energy range 2−15 keV and 15−30 keV, we utilize standard `FTOOLS` tasks, namely `saextrct` for Binned mode data and `seextrct` for Event mode and Good Xenon data (see Nandi et al. 2012; Radhika & Nandi 2014, and references therein). Subsequently, we use `lcmath` task to merge two lightcurves to obtain the resultant lightcurve in $2-30$ keV energy range in obtaining the power density spectrum.

For wide-band ($3-100$ keV) spectral modelling, we utilize `Standard2` data products from PCA and extract the source spectrum, background spectrum and response file using standard `FTOOLS` tasks, such as `seextrct`, `pcabackest` and `pcarsp`, respectively. In order to generate the background spectrum for PCA data, we use the bright background model[3] and SAA passage history from SAA webpage[4]. In case of HEXTE data, we separate the source and background raw FITS file from Science data product using `hxtback` task for all sources. We extract the source and background spectra, perform the deadtime correction and finally generate the response file using `seextrct`, `hxtdead` and `hxtrsp` tasks, respectively.

The *Hard X-ray Modulation Telescope* also known as *Insight-HXMT* (Zhang et al. 2014) comprises of three instruments: low-energy X-ray telescope (LE: $1-15$ keV; Chen et al. (2020)), medium-energy X-ray telescope (ME: $5-30$ keV; Cao et al. (2020)) and high-energ X-ray telescope (HE: $20-250$ keV (Liu et al. 2020)). We utilize data from all three instruments for our spectro-temporal analysis of Swift J1727.8−1613, MAXI J1535 − 571 and Swift J1658.2 − 4242. However, data beyond MJD 60222 for Swift J1727.8 − 1613 is not available due to Sun constrain (Yu et al. 2024). We use the `hpipeline` under *Insight-HXMT* Data Analysis Software (`HXMTDAS`) version v2.06 to reduce the data. Data extraction is done using the criteria recommended by the *Insight-HXMT* team, *i.e.*, pointing offset $\leq 0.04^{\circ}$, Earth elevation angle $\geq 10^{\circ}$, geomagnetic rigidity cut-off value ≥ 8 GV and finally, 300 s before and after SAA. Similar to data from *RXTE*, the lightcurve is generated with time resolution 8 ms from energy range $2-30$ keV.

AstroSat, India's first dedicated multiwavelength space observatory launched in 2015, is equipped with a suite of X-ray instruments, including the Soft X-ray Telescope (*SXT*) (Singh et al. 2017), the Large Area X-ray Proportional Counter (*LAXPC*) (Yadav et al. 2016; Antia et al. 2017), and the Cadmium Zinc Telluride Imager (*CZTI*) (Yadav et al. 2016). For the present study, we employed the *LAXPC10* and *LAXPC20* detectors for timing analysis of Swift J1658.2–4242, and used only *LAXPC20* for spectral analysis. The *LAXPC* instrument is sensitive to X-rays in the $3-80$ keV energy range (Yadav et al. 2016; Agrawal et al. 2017; Antia et al. 2017). Data reduction from level-1 to level-2 was carried out using `LAXPCSoftv3.4.4`[5], the latest software package released on June 21, 2023 (Antia et al. 2017).

2.2 Radio Data

We compile the radio flux data for BH-XRBs from the existing literature. In particular, observations of the source XTE J1859+226 across a range of radio frequencies are obtained from Brocksopp et al. (2002), and due to dense coverage within the $1.4-1.66$ GHz band, we focus solely on radio fluxes within this frequency range for our analysis. The radio flux for XTE J1550−564 is obtained from Hannikainen et al. (2001) at 8.6 GHz. Radio flux data for 4U 1543−47 is obtained from Park et al. (2004); Kalemci et al. (2005). Radio flux values from the 2009 outburst of H1743−322 are extracted from Miller-Jones et al. (2012). We use radio flux for XTE J1752−223 from Brocksopp et al. (2013). For XTE J1650−500, radio flux values are taken from Corbel et al. (2004). For GX 339−4, we utilize radio fluxes from its 2002, 2007 and 2010 outbursts as reported by Gallo et al. (2003) and Corbel et al. (2013); Islam & Zdziarski (2018). Radio observations of XTE J1748−288 are taken from Brocksopp et al. (2007), and for GRO J1655−40, we adopt the flux values from Shaposhnikov et al. (2007). MAXI J1535−571 and Swift J1658.2−4242 radio fluxes are obtained from Russell et al. (2019) and Bogensberger et al. (2020), respectively. Radio flux for Swift J1753.5−0127 is obtained from Soleri et al. (2010) and lastly, the radio observations in Swift J1727.8−1613 are taken from Peters et al. (2023). Moreover, flux values for the 2003 outburst of H1743−322 are explicitly used for jet velocity calculation (McClintock et al. 2009). Note that to estimate the jet velocity, we normalize the radio flux values for 5 GHz as,

$$\mathrm{F}(5\ \mathrm{GHz}) = \mathrm{F}(\nu) \times \left(\frac{5\ \mathrm{GHz}}{\nu}\right)^{\alpha}, \tag{1}$$

where α denotes the spectral index and ν is the frequency of observation.

3 ANALYSIS AND MODELLING

We revisit the archival data of thirteen outbursting BH-XRBs and carry out the spectro-temporal analysis of these sources

[3] https://heasarc.gsfc.nasa.gov/docs/xte/pca_bkg_epoch.html
[4] https://heasarc.gsfc.nasa.gov/docs/xte/pca_history.html
[5] https://www.tifr.res.in/~AstroSat_LAXPC/LAXPCSoft.html

to extract key timing and spectral parameters. This comprehensive approach enables us to explore the underlying disc-jet connection, likely driven by the complex accretion processes occurring around these sources.

3.1 Timing Analysis

We generate the power density spectrum (PDS) from $2-30$ keV lightcurve in rms space using `powspec` task and apply norm $=-2$ to remove the Poisson noise. The QPO feature is modelled in `XSPEC` environment (`v12.14.0`) using multiple `Lorentzian` and `powerlaw` model components. With this, we estimate total rms in the frequency range $0.01-62.5$ Hz and QPO rms as $\mathrm{rms_{QPO}}\% = \sqrt{P \times \Delta\nu} \times 100$, where P denotes the power in the unit of $\mathrm{rms^2\ Hz^{-1}}$ and $\Delta\nu$ is the width of the frequency bin (Riemann 2004; Belloni & Hasinger 1990; Radhika et al. 2018; Bhuvana et al. 2021).

Time lag analysis is performed by generating lightcurves in the energy ranges $2-6$ keV and $6-15$ keV, with the $2-6$ keV lightcurve serving as the reference energy band. The simultaneous photon counts of the lightcurves in these two energy bands at time $t_{\rm k}$ are denoted as $x_{\rm a}(k)$ and $x_{\rm b}(k)$. Their Fourier transforms are given by (van der Klis 1988; Majumder et al. 2024),

$$X_a(j) = \sum_{k=0}^{N-1} x_a(k) \exp(2\pi i \nu_j t_k), \tag{2}$$

$$X_b(j) = \sum_{k=0}^{N-1} x_b(k) \exp(2\pi i \nu_j t_k), \tag{3}$$

where $x_a(k) \equiv x_a(t_k)$ and $X_a(j) \equiv X_a(\nu_j)$. Here, k and j represent the time and frequency bins, such that $k \in [0, N-1]$ and $j \in [-N/2, N/2-1]$. In addition, N indicates the total number of bins of the time series having time length T and time step $\delta \mathrm{t} = T/N$. Thus, $t_k = kT/N$ refers time in $k_{\rm th}$ bin and $\nu_j = j/T$ denotes frequency at $j_{\rm th}$ bin of the equidistant time and frequency series data.

Cross spectrum between these two Fourier transforms is given as $C(j) = X_a^*(j) X_b(j)$ (Nowak et al. 1999), where $X_a^*(j)$ is the Fourier transform of $2-6$ keV light curve and $X_b(j)$ is the Fourier transform of $6-15$ keV lightcurve at frequency ν_j. The phase lag is given by the argument/position angle of $C(j)$ in the complex plane and is calculated as,

$$\phi = arg[C(j)]. \tag{4}$$

Finally, the time lag at the QPO frequency ν_j is estimated as,

$$\delta t(j) = \frac{C(j)}{2\pi\nu_j}. \tag{5}$$

The time lag is computed as the average over the frequency range $\nu_{\rm QPO} \pm$ FWHM (Reig et al. 2000), where FWHM denotes the full width at half maximum of the QPO. To calculate the time lag energy spectrum, the $2-6$ keV band is selected as the reference, with $6-10$ keV, $10-15$ keV, $16-20$ keV, $20-24$ keV, and $24-30$ keV as the subject bands. The time lag is calculated using the Stingray `v.1.1.2` module (Huppenkothen et al. 2019) in the `astropy` package of Python.

3.2 Spectral Analysis

We perform wide-band $(3-100$ keV) spectral modeling using data from the PCA $(3-40$ keV) and HEXTE $(20-100$ keV) instruments of the *RXTE* mission. We use data from PCU-2/PCA and Cluster-A/HEXTE for all observations of all sources under considerations except for 2009 outburst of H1743−322, where Cluster-B data are analyzed. For *Insight/HXMT* observations, we use LE (2−10 keV), ME (8−35 keV) and HE $(28-120$ keV) for broadband spectral analysis. In case of *AstroSat*, we use *LAXPC20* $(3-60$ keV) for spectral analysis. Throughout the analysis, 1% systematic error is considered for spectral modeling using `XSPEC` (`version` 12.14.1`d`).

In order to carry out the spectral modeling, we first adopt a model combination `tbabs`×`(diskbb+cutoffpl)`×`constant`. The model component `tbabs` (Wilms et al. 2000) is used to explain the interstellar absorption. The thermal and non-thermal emissions of the accretion disc are taken care by the model components `diskbb` (Makishima et al. 1986) and `cutoffpl`. We use this model combination for the spectral fitting of one BH-XRB (as an example XTE J1859+226) that yields reasonable fit with $\chi^2_{red} \sim 0.7-1.4$ for most of the observations. We obtain $E_{\rm cut} \sim 50-90$ keV in LHS and HIMS. In SIMS and HSS, $E_{\rm cut}$ could not be directly constrained, and hence, we perform spectral modelling by fixing $E_{\rm cut}$ at discrete values in 5 keV intervals. The optimal $E_{\rm cut}$ is identified as the value that yielded the least variations in $\chi^2_{\rm red}$. Based on this analysis, $E_{\rm cut}$ is fixed in the range $\sim 50-60$ keV for SIMS and ~ 10 keV for HSS. However, `cutoffpl` being a phenomenological model failed to quantify certain physical parameters, such as scattering fraction and electron temperature.

Hence, we adopt the convolution model `thcomp` (Zdziarski et al. 2020) that successfully explains the spectral characteristics at high energies for BH-XRBs under considerations. Accordingly, we use a model combination `tbabs`×`(thcomp`⊗`diskbb)`×`constant`. To account for the reflection and absorption features, we use `Gaussian` in the energy range $6-7$ keV, and `smedge` (Ebisawa et al. 1994) based on its usefulness in previous studies (Sobczak et al. 1999; Tomsick & Kaaret 2000; Yamaoka et al. 2012; Aneesha et al. 2019; Dong et al. 2020). Note that `Gaussian` model suffices for all BH-XRBs except XTE J1859+226, where both `Gaussian` and `smedge` are required to obtain best fit (Radhika & Nandi 2014; Nandi et al. 2018). The spectral modeling yields spectral index Γ in the range $1.6-1.8$ during LHS for all sources. Notably, we are unable to constrain electron temperature kT_e for number of observations during SIMS, and hence, we freeze kT_e to obtain the best fit. In doing so, we perform multiple spectral fits by fixing kT_e at discrete intervals of 5 keV as before, and select the value of kT_e[1] with minimal change in $\chi^2_{\rm red}$. The `cov_frac` is computed respectively as ~ 0.8 in LHS, $\sim 0.4-0.5$ in SIMS and $\lesssim 0.02$ in HSS for all sources under considerations. However, for Swift J1727.8−1613, we adopt a model combination with an additional cutoff power-law component to compensate for high energy excess following Yang et al. (2024) as

[1] For type-A and type-B QPOs, acceptable fits are obtained by fixing $kT_e \sim 10-20$ keV in SIMS.

`tbabs×(thcomp⊗diskbb+ga+cutoffpl)×constant`. We calculate the bolometric luminosity, and estimate the normalized Comptonized flux ($F_{\rm nth}$, ratio between the Comptonized flux and the total flux) and normalized disc flux (ratio between the disc flux and the total flux) for the energy range of $1-100$ keV.

We put efforts to estimate the spin of nine black hole sources using continuum fitting. We employ relativistic accretion disc model `kerrbb2` (McClintock et al. 2006) and calculate the black hole spin considering the hardening factor lies between $1.4-2$ (Davis et al. 2005; Davis & El-Abd 2019). With this, we adopt a model combination as `tbabs×(simpl⊗kerrbb2)×constant`, where `simpl` is used for fitting the Comptonization component of the energy spectrum (Steiner et al. 2009). Observations in the HSS are considered for modeling if the scattering fraction, $f_{\rm scat}$, is less than or equal to 25% (Steiner et al. 2011). However, this modeling does not apply to Swift J1753.5−0127, Swift J1727.8−1613, MAXI J1535 − 571 and Swift J1658.2 − 4242 as the conditions required were not satisfied in any of their observations.

4 RESULTS

4.1 Outburst Profile and Hardness Intensity Diagram

In Fig. 1, we present the outburst profiles of thirteen BH-XRBs under consideration, where bolometric ($1-100$ keV) X-ray fluxes are plotted as function of day (in MJD) starting from the beginning of the outburst (T_0). Open symbols connected with dotted lines denote the outburst profile for GX 339 − 4 (red, cyan and blue for 2002, 2007 and 2010 outbursts), 4U 1543−47 (orange; 2002 outburst), Swift J1753.5−0127 (yellow; 2005 outburst), XTE J1752−223 (pink; 2009 outburst), XTE J1650−500 (light green; 2001 outburst), XTE J1859+226 (red; 1999 outburst), H1743−322 (cyan; 2009 outburst), XTE J1550−564 (blue; 1998 outburst), Swift J1727.8−1613 (orange; 2023 outburst), XTE J1748-288 (yellow; 1998 outburst), GRO J1655 − 40 (pink; 2005 outburst), MAXI J1535 − 571 (light green; 2017 outburst) and Swift J1658.2−4242 (grey; 2018 outburst) sources, respectively. 'Plus' symbol indicates the time of radio flares observed during an outburst. At the inset, we depict HID for all the sources using same point styles and colors as used for displaying outburst profiles.

During 1999 outburst, XTE J1859+226 traced all the canonical spectral states, such as LHS, HIMS, SIMS and HSS, in its hysteresis loop depicted by open circles (in red) in HID of Fig. 1. The source exhibited its peak X-ray flux ($\sim 6\times10^{-8}$ erg s^{-1}cm^{-2}) along with multiple radio flares (Brocksopp et al. 2002; Fender et al. 2009; Radhika & Nandi 2014) during SIMS (HR $\lesssim 0.7$) as indicated by 'plus' symbol in Fig. 1 and dotted vertical lines (marked as F1, F2, F3 and F4) in Fig. 2. We observe a slight increase in X-ray flux preceding each radio flare. Similar to XTE J1859+226, GX 339−4 during its 2002, 2007 and 2010 outburst traced all canonical spectral states. It exhibited one X-ray peak in 2007 and 2010 outbursts with X-ray fluxes $\sim 3.3\times10^{-8}$ erg s^{-1} cm^{-2} and $\sim 2.6\times10^{-8}$ erg s^{-1} cm^{-2}, respectively. During its 2002 outburst, it exhibited two peaks in X-rays (during SIMS with flux ($\sim 3.5\times10^{-8}$ erg s^{-1}cm^{-2} and HSS with flux $\sim 5.0\times10^{-8}$ergs^{-1}cm^{-2}), however radio flare is observed ~ 3 days before the X-ray peak in SIMS (HR ~ 0.6; Fig. 1 and Fig. 4). The source 4U 1543−47 was observed in SIMS while transiting from HIMS, showing a single X-ray peak ($\sim 1.7\times10^{-7}$ erg s^{-1}cm^{-2}) during SIMS, with a radio flare observed approximately 2 days before the peak X-ray flux (HR ≥ 0.1; Fig. 1 and Fig. 6). H1743−322 is seen to transit from HIMS to SIMS with a peak X-ray flux ($\sim 1.6\times10^{-8}$ erg s^{-1}cm^{-2}) during SIMS. As before, we find that the radio flare occurs ~ 1 day after the peak X-ray flux at HR ~ 0.6 (see Fig. 1). Similar to GX 339−4, XTE J1550−564 also evolved from HIMS to SIMS with multiple X-ray peaks ($\sim 2.8\times10^{-7}$ erg s^{-1}cm^{-2} during SIMS and $\sim 1.3\times10^{-7}$ erg s^{-1}cm^{-2} during HSS). The radio flare is observed approximately 1 day after the peak X-ray flux in the SIMS phase, when the hardness ratio (HR) is $\gtrsim 0.8$ (see Fig. 1).

The source XTE J1752−223 exhibited an outburst in 2009, but due to Sun constraints, no observations were available from MJD $55155.09-55215.90$. During its outburst, the source reached a peak X-ray flux of $\sim 5\times10^{-8}$ erg s^{-1} cm^{-2}, accompanied by multiple radio flares (Brocksopp et al. 2013) in the SIMS, HSS, and during the transition from SIMS to HIMS in the decay phase. XTE J1752−223 displayed all canonical spectral states, with marginal rise in X-ray flux near the radio flares. XTE J1650−500 was also observed in all canonical spectral states with the peak X-ray flux of 4×10^{-8} erg s^{-1} cm^{-2} occurring during SIMS. The peak radio flux of ~ 5.28 mJy at 4.8 GHz was observed during HIMS, though radio observations were absent during the transition from HIMS to SIMS, potentially missing the flare event (Fender et al. 2009). Swift J1753.5−0127 underwent a failed outburst and evolve from HIMS to LHS in the HID. Similar to other canonical outbursting sources, the peak radio flux of 2.48 mJy at 8.4 GHz coincided with the X-ray peak flux of 2×10^{-8} erg s^{-1} cm^{-2}. Recently, Swift J1727.8−1613 exhibited the highest X-ray flux among the sources, reaching a peak of $\sim 3.5\times10^{-7}$ erg s^{-1} cm^{-2}. Multiple radio flares (≥ 100 mJy at 334 MHz) were observed as the source transits to SIMS. For GRO J1655−40, the source exhibits all four canonical spectral states, with two distinct peaks in X-ray flux: $\sim 6.4\times10^{-8}$ erg s^{-1} cm^{-2} during SIMS and $\sim 9.5\times10^{-8}$ erg s^{-1} cm^{-2} during HSS. XTE J1748−288 also makes transition through all four spectral states, reaching a peak X-ray flux of $\sim 2.5\times10^{-8}$ erg s^{-1} cm^{-2}. MAXI J1535−571 is observed in LHS, HIMS, SIMS, and HSS with a maximum X-ray flux of $\sim 22\times10^{-8}$ erg s^{-1} cm^{-2} during SIMS. Swift J1658.2−4242, on the other hand, is observed during the HIMS and SIMS phases, exhibiting a peak X-ray flux of $\sim 3.1\times10^{-8}$ erg s^{-1} cm^{-2}.

It is worth mentioning that XTE J1859+226, H1743−322, XTE J1550−564, Swift J1727.8−1613, XTE J1748 − 288, GRO J1655−40, MAXI J1535−571 and Swift J1658.2−4242 are high-inclination sources ($i \geq 60^\circ$) (Hynes et al. 2002; Zurita et al. 2002; Jonker & Nelemans 2004; Shafee et al. 2006; Jonker et al. 2010; Orosz et al. 2011; Steiner et al. 2012; Corral-Santana et al. 2013; van den Eijnden et al. 2017; Miller et al. 2018; Xu et al. 2018; Yanes-Rizo et al. 2022; Wood et al. 2024; Yu et al. 2024; Abdulghani et al. 2024), and these sources typically show radio flares about one day after the X-ray peak in SIMS. In contrast, GX 339−4, 4U 1543−47,

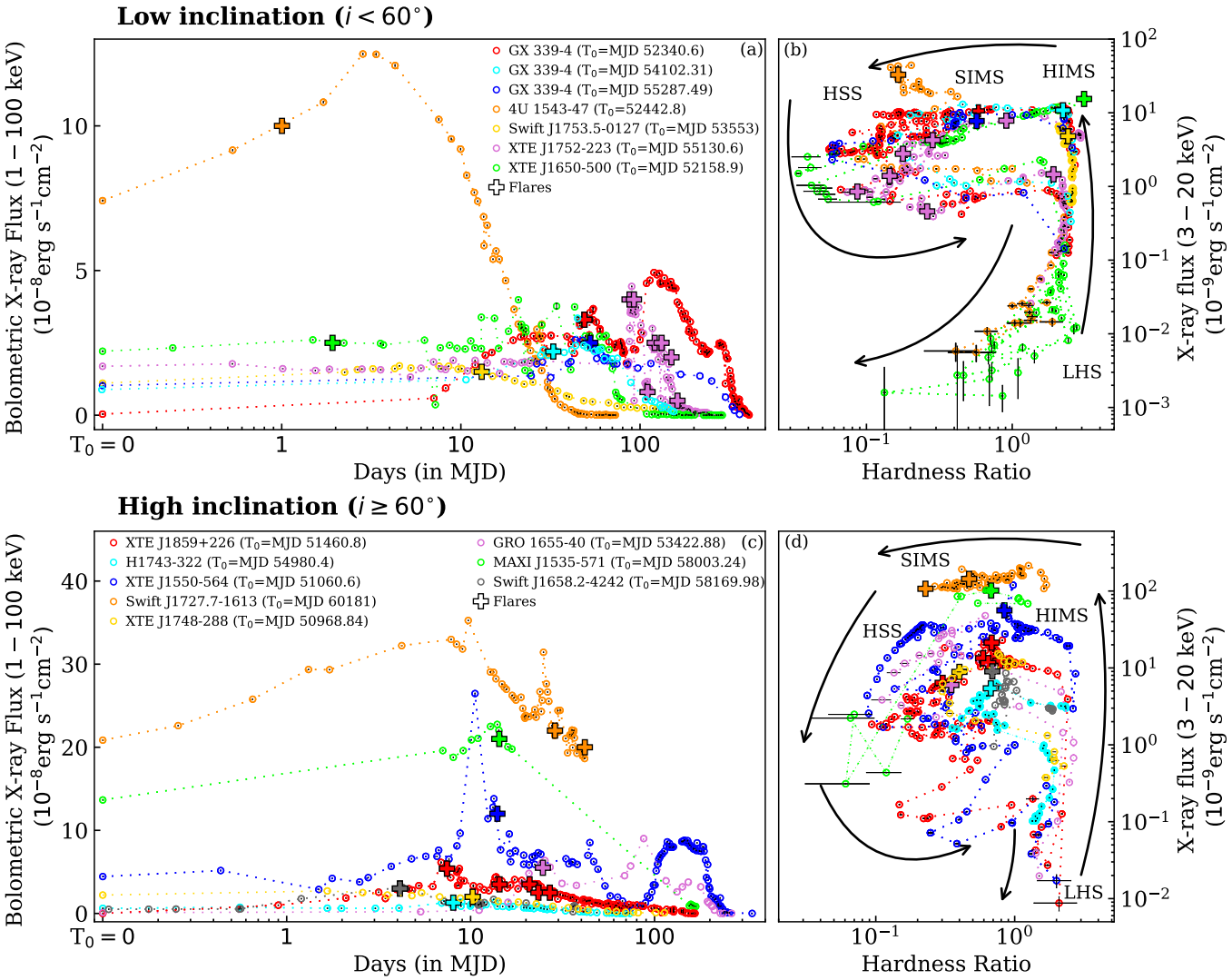

Figure 1. Evolution of (a) bolometric (1 − 100 keV) X-ray flux in low inclination sources such as GX 339 − 4 (outbursts in 2002, 2006 and 2010 represented by red, cyan and blue symbols, respectively), 4U 1543 − 47 (orange), Swift J1753.5 − 0127 (yellow), XTE J1752 − 223 (pink) and XTE J1650 − 500 (light green) and (c) in high inclination sources such as XTE J1859 + 226 (red), H1743 − 322 (2009 outburst) (cyan), XTE J1550 − 564 (blue), Swift J1727.8 − 1613 (orange, using HXMT data), XTE J1748 − 288 (yellow), GRO J1655 − 40 (pink), MAXI J1535 − 571 (light green using HXMT data) and Swift J1658.2 − 4242 (grey, using AstroSat and HXMT data). The start date of the outbursts is denoted by T_0. The hardness intensity diagram (HID) for both low and high-inclination sources are illustrated in (b) and (d), respectively. The radio flares are marked using the 'plus' symbol in the outburst profile and HID. See the text for details.

XTE J1752−223, XTE J1650−500, and Swift J1753.5−0127 are low-inclination sources with $i \sim 35° - 50°$.

4.2 Evolution of Spectro-temporal Properties During Jet Ejection

In this section, we study the evolution of spectro-temporal parameters during the entire outburst of all the sources under consideration (XTE J1859 + 226, GX 339 − 4 (2002, 2007 and 2010 outbursts), 4U 1543 − 47, H1743 − 322 (2009 outburst), XTE J1550 − 564, XTE J1752 − 223, XTE J1650 − 500, Swift J1753.5 − 0127, XTE J1748 − 288, GRO J1655 − 40, Swift J1727.8 − 1613, MAXI J1535 − 571 and Swift J1658.2 − 4242.) In Fig. 1, we denote the peak radio flux with 'plus' symbol which indicates the presence of the radio ejection in SIMS (as shown in the inset).

In Fig. 2, we present the evolution of spectro-temporal parameters of XTE J1859+226 during 1999 outburst. We depict the evolution of Radio flux, bolometric X-ray flux, Flux ratios (normalized disc and Comptonized fluxes), photon index (Γ), covering fraction (cov_frac), centroid frequency ($\nu_{\rm QPO}$), QPO rms (rms$_{\rm QPO}$%), total rms (rms$_{\rm Total}$%) and time lag at QPO frequency with time since the triggering of the outburst. XTE J1859+226 exhibits four radio flares (marked as F1, F2, F3 and F4 at the top of Fig. 2) along with X-ray peaks during SIMS (see Fig. 1).

During the rising phase of the outburst, XTE J1859+226 exhibits type-C QPOs (evolves from 0.45−6.20 Hz) with weak variation of radio emission (∼ 10 mJy). When the source

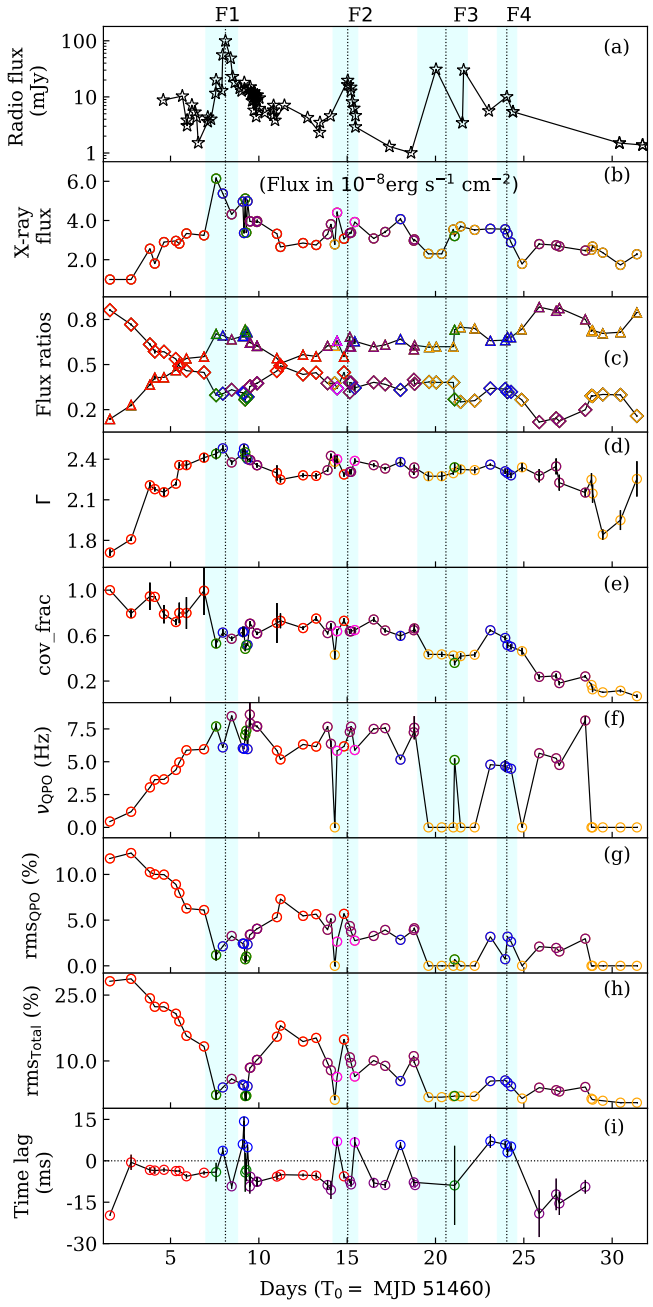

Figure 2. Evolution of (a) Radio flux in $1.4 - 1.66$ GHz (asterisk), (b) bolometric X-ray flux ($1-100$ keV), (c) Flux ratios (normalized disc flux (triangle) and normalized Comptonized flux (diamond)), (d) photon index (Γ), (e) covering fraction (cov_frac), (f) centroid frequency of QPO ($\nu_{\rm QPO}$), (g) QPO rms ($\rm rms_{QPO}$), (h) total rms ($\rm rms_{Total}$), and (i) time lag at QPO frequency between energy range $6 - 15$ keV and $2 - 6$ keV of XTE J1859+226 during its 1999 outburst. Data points plotted with various colors represent different types of QPO (green: type-A QPO, blue: type-B QPO, magenta: type-B cathedral, red: type-C QPO and purple: type-C* QPO, orange: absence of QPO). The vertical dotted lines represent the peak of radio flares. Shaded regions represent the flaring zone consisting of rising phase, peak value and declining phase of radio flux in a particular flare. See the text for details.

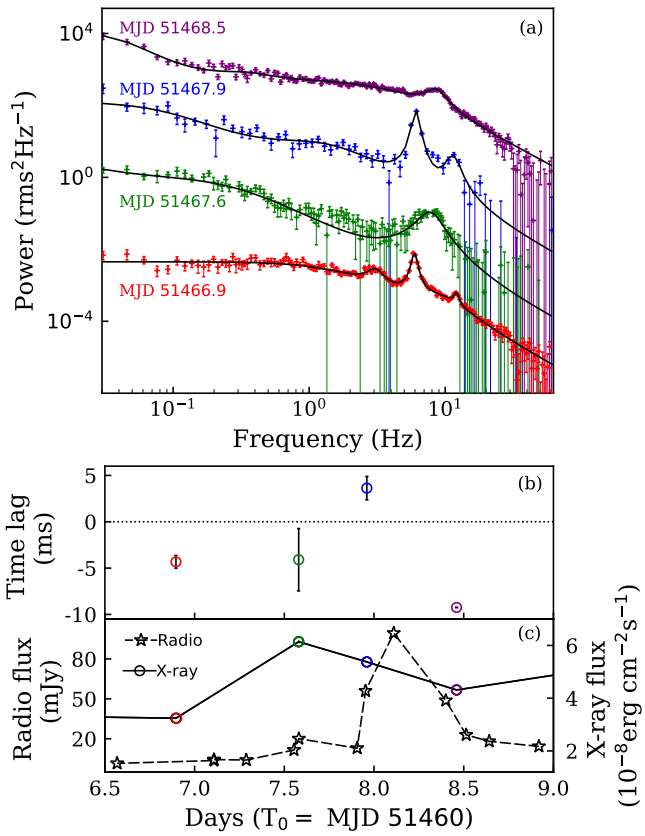

Figure 3. Evolution of (a) PDS (scaled for better clarity), (b) time lag (open circle) corresponding to different types of QPOs, and (c) bolometric X-ray flux (open circle) and Radio flux in $1.4 - 1.66$ GHz (asterisk) near flare F1 (MJD 51467.9) of XTE J1859+226. Different colors denote various types of QPO (green: type-A, blue: type-B, red: type-C and purple: type-C*). See the text for details.

transits from HIMS to SIMS, a type-A QPO appears along with a peak X-ray flux ($\sim 6.14 \times 10^{-8}$ erg cm^{-2} s^{-1}) and enhanced radio flux 100 mJy, indicating radio ejection marked as F1 (see also Fig. 3). It's worth noting that type-B/B-cathedral QPOs appear about $3 - 10$ hours before the radio flares F1, F2, F3, F4, which are marked by a positive time lag of around $5 - 8$ ms. Generally, observations show type-A QPOs, weak type-C* QPOs, or the absence of QPOs prior to the appearance of type-B QPOs, with $\rm rms_{QPO}$% around 1.0%, compared to 2.5% for type-B QPOs. In addition, type-A and type-C* QPOs are associated with a negative time lag of ~ 5 ms. Throughout the flaring periods, the disc flux (≥ 0.5) is observed to dominate over the Comptonized X-ray flux. Next, we focus on the evolution of PDS during the radio flare, specifically for flare F1, and examine how it correlates with variations in radio flux, X-ray flux, and time lag (see Fig. 3). As the source transits from HIMS to SIMS, it exhibits a type-C QPO on MJD 51466.9, followed by a type-A QPO on MJD 51467.6, type-B on MJD 51467.9 and type-C* on MJD 51468.5, respectively (see panel a). The time lag in these four observations flips from negative to positive (see panel (b)), coinciding with the onset of a radio flare. As QPO type alters from type-A to type-B, both X-ray flux (depicted by open circles) and radio flux (marked by asterisks) increases (see panel c). These results possibly suggest a change in the

accretion dynamics in the vicinity of the source under consideration. After $\sim$ 10 hrs, the nature of the QPO is again altered to type-C* yielding a negative time lag. Similar time lags associated with type-B QPOs are also observed for F2, F3 and F4 radio flares as well. Although the type-A QPO is observed before the radio ejection, type-B QPOs are observed with positive time lag for all four radio flares.

We investigate the remaining seven high-inclination sources, namely H1743−322 (Steiner et al. 2012; Molla et al. 2017), XTE J1550−564 (Jonker & Nelemans 2004; Jonker et al. 2010; Orosz et al. 2011), Swift J1727.8−1613 (Wood et al. 2024; Yu et al. 2024), GRO J1655 − 40 (Markwardt & Swank 2005), XTE J1748 − 288 (Brocksopp et al. 2007), MAXI J1535 − 571 (Negoro et al. 2017) and Swift J1658.2 − 4242 (Grebenev et al. 2018). During the initial phase of 2009 outburst of H1743−322, type-C QPOs are observed in HIMS with $\nu_{\rm QPO}$ increasing from 0.9 − 3.6 Hz. Subsequently, type-A QPO appears as the sources transits from HIMS to SIMS. The appearance of type-A QPO ($\nu_{\rm QPO} \sim 3.4$ Hz, ${\rm rms_{QPO}}\% \sim 2\%$ and ${\rm rms_{Total}}\% \sim 6.1\%$) during state transition coincides with the observation exhibiting the peak X-ray flux in the entire outburst. After $\sim$ 1 day, the radio flare ($\sim$ 7 mJy at 8.46 GHz) is observed. The subsequent observation in X-ray band does not exhibit QPO in the PDS followed by type-C* QPO ($\nu_{\rm QPO} \sim 6.8$ Hz, ${\rm rms_{QPO}}\% \sim 2.5\%$ and ${\rm rms_{Total}}\% \sim 6.6\%$) and type-B QPO ($\nu_{\rm QPO} \sim 3.7$ Hz, ${\rm rms_{QPO}}\% \sim 3.5\%$ and ${\rm rms_{Total}}\% \sim 7.2\%$). Type-C, type-C* and type-A QPOs display negative time lags ($\sim 0.3 - 2$ ms, $\sim$ 3 ms and $\sim$ 10 ms), whereas type-B QPOs demonstrate positive time lag ($\sim 5 \pm 2.8$ ms) during 2009 outburst. The appearance of type-A QPO during the state-transition corresponding to the peak X-ray flux just before the appearance of radio flare marks the onset of ejection phenomena.

During 1998 outburst, XTE J1550−564 underwent spectral state transition from HIMS to SIMS with the detection of radio flare (234 mJy at 8.6 GHz) and appearance of type-A QPO ($\nu_{\rm QPO} \sim 12$ Hz and ${\rm rms_{QPO}}\% \sim 0.5\%$ and ${\rm rms_{Total}}\% \sim 2\%$). Type-C QPO again appears in the PDS after the radio flare, with $\nu_{\rm QPO}$ decreasing from $\sim$ 5.4 Hz to $\sim$ 2.6 Hz, then rising again from $\sim$ 2.7 Hz to $\sim$ 5.2 Hz. Interestingly, type-A and type-B QPOs re-appear in the PDS just before the source transits from SIMS to HSS, with $\nu_{\rm QPO}$ values of $\sim$ 6.9 Hz and $\sim$ 4.5 Hz, respectively. The time lag associated with type-C QPOs varies between positive and negative values, while the type-A QPOs show a negative lag of $\sim$ 5 ms, and type-B QPOs exhibit time lag as -2.3 ± 1.6 ms (MJD 51106.95), 1.7 ± 0.5 ms (MJD 51108.07) and -4.0 ± 2.6 ms (MJD 51110.26), respectively.

Swift J1727.8−1613 shows type-C QPOs with monotonically increasing frequency as 0.37 − 8.74 Hz before F1 radio flare (Nandi et al. 2024) during 2023 outburst. The appearance of the type-B ($\nu \sim 6.97$ Hz, ${\rm rms_{QPO}}\% \sim 4.91\%$) QPO on MJD 60206.13, prior to F1, suggests that this observation marks the transition from HIMS to SIMS as indicated by Nandi et al. (2024) based on the HR value $\sim 0.19 - 0.02$ using *MAXI/GSC* observations. After F1, $\nu_{\rm QPO}$ increases till 8.85 Hz and finally disappears before F2 (see Fig. 6). We observe both positive and negative time lags associated to type-C QPOs with high normalized Comptonized flux ($F_{\rm nth}$) (see Fig. 7).

Next, we examine the spectro-temporal characteristics of low-inclination source, namely GX 339−4. We find that

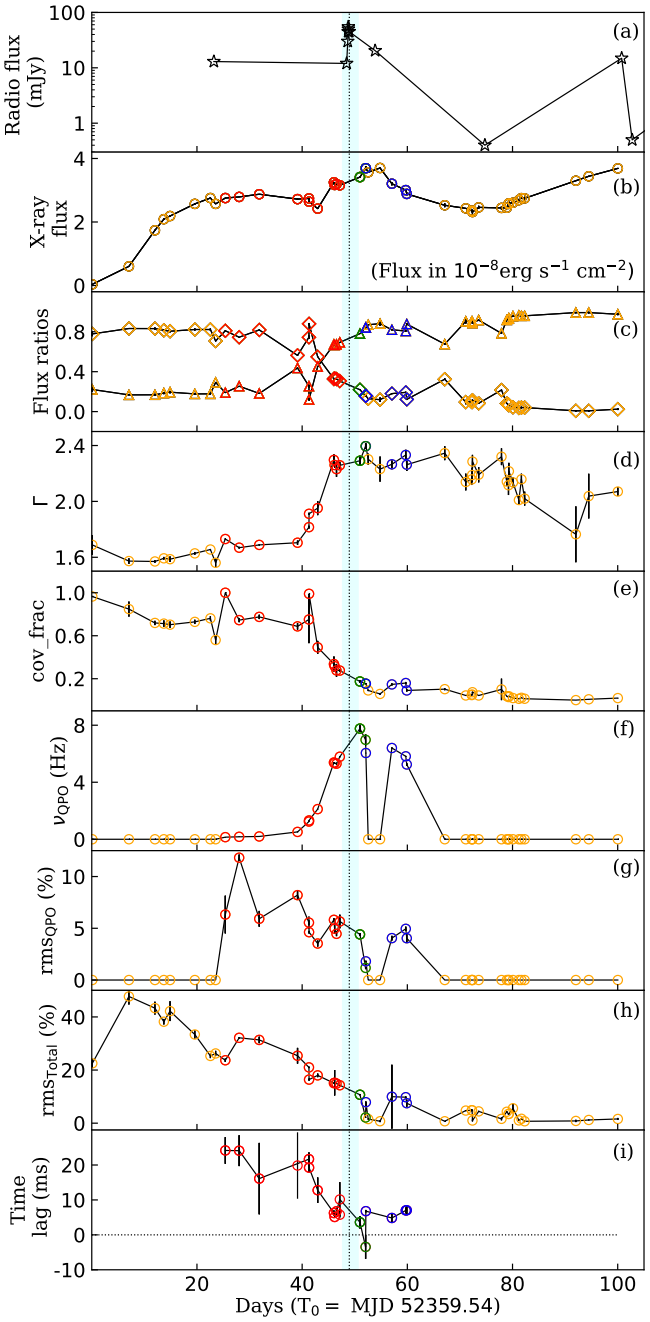

Figure 4. Same as Fig. 2, but for GX 339−4 during its 2002 − 2003 outburst. See the text for details.

GX 339−4 exhibits only one radio flare during the entire 2002 − 2003 outburst. In Fig. 4, we present the evolution of the timing as well as spectral parameters obtained during the outburst. As the outburst progresses, the frequency of type-C QPOs increases with the enhancement of the X-ray flux with peak value $\sim 3.5 \times 10^{-8}$ erg s^{-1}cm^{-2}. During the transition from HIMS to SIMS, radio flare is observed with peak flux (55 mJy) and type-A QPO appears followed by type-B QPO. It is worth mentioning that the time lag decreases from $\sim$ 21 ms to ~ -3.5 ms, where negative lag is observed corresponding to one of the type-A QPOs. Furthermore, we notice that the normalized Comptonized flux and

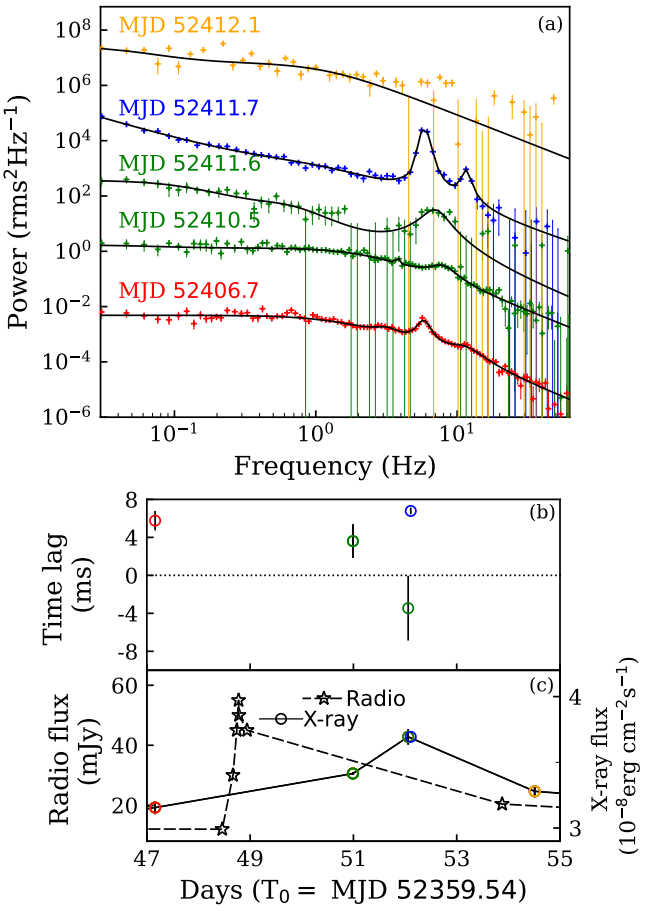

Figure 5. Evolution of (a) PDS (scaled for better clarity), (b) time lag (open circle) corresponding to different types of QPOs, and (c) bolometric X-ray flux (open circle) and Radio flux at 4.8 GHz (asterisk) near flares (MJD 52408.31) of GX 339−4. Different colors denote various types of QPO (green: type-A, blue: type-B, red: type-C and orange: absence of QPO. See the text for details.

disc flux alter before the radio flare. In Fig. 5, we depict the evolution of the PDS along with the X-ray and radio fluxes during the radio flare (MJD 52410.5 to MJD 52412.1) of GX 339−4. We observe that type-A and type-B QPO emerge ~ 2 days after the radio flare. We infer that this delay possibly arises due to a lack of X-ray monitoring. Furthermore, we also analyzed 2007 and 2010 outbursts of GX 339−4 and the obtained results are presented in Figs. 6-8.

4U 1543−47 is another low-inclination source with $i \sim 20°-40°$ (Orosz et al. 1998; Chen & Wang 2024). During 2002 outburst, the source transits from HIMS to SIMS exhibiting peak X-ray flux ($\sim 12.5 \times 10^{-8}$ erg s^{-1} cm^{-2}) accompanied by a radio flare (~ 22 mJy at 1026.75 MHz). After the radio flare, QPO disappears from the PDS. A subsequent weak radio flare (≤ 0.3 mJy) was detected (Russell et al. 2020), and type-A and type-B QPOs were observed near the time of the radio flare (see Fig. 6). Type-B QPO displays positive time lags ($\sim 2.3-6.2$ ms) and type-A QPO is observed with negative time lags ($\sim 1.7-5.5$ ms). Note that a type-C QPO of $\nu_{\rm QPO} \sim 9$ Hz is observed towards the end of the outburst.

XTE J1650−500 exhibits a canonical outburst, with the peak radio flux of approximately ~ 5.3 mJy at 4.8 GHz and a spectral index of ~ -0.27 observed during the hard intermediate state (HIMS). Type-C QPOs are observed to evolve with $\nu_{QPO} \sim 0.97-6.88$ Hz. Near the HIMS to SIMS transition, type-B QPOs ($\nu_{\rm QPO} \sim 16-17$ Hz, rms$_{\rm QPO} \sim 3\%$) appear and then disappear in the PDS, with no radio observations available near the transition (see Fig. 6). Both type-C and type-B QPOs exhibit a positive lag.

Swift J1753.5−0127 displays a failed outburst, remaining in LHS and HIMS, with its HID mimicking the decay phase of a canonical outburst (see Fig. 1). At the beginning of the outburst, the source is in HIMS, as indicated by its high bolometric flux ($\geq 1.0 \times 10^{-8}$ erg cm^{-2} s^{-1}) and HR (≤ 2.4). The peak radio flux (≥ 1.5 mJy at 8.4 GHz with a spectral index of ~ -0.08) is observed near the peak X-ray flux. The source transits into LHS during the decay phase of the outburst. Type-C QPOs are observed with positive time lags throughout the outburst and $\nu_{\rm QPO}$ is seen to increase from 0.60 Hz to ~ 0.85 Hz at the beginning and then decreases during the decay phase.

XTE J1748−288 underwent a canonical outburst during its 1998 outburst. Observations commenced while the source was in HIMS, during which it exhibited a peak bolometric X-ray flux of $\sim 2.7 \times 10^{-8}$ erg s^{-1} cm^{-2}. At the onset of the outburst, the PDS revealed the presence of type-C QPO with centroid frequencies in the range $\nu \sim 17-31$ Hz and fractional rms amplitudes of $\sim 1.7\%-4.3\%$. The Q factor associated with these QPOs spans $\sim 3-12$. Note that the QPOs vanish from the PDS prior to the detection of a radio flare.

During its 2005 outburst, GRO J1655−40 exhibited all four canonical spectral states, reaching a peak bolometric X-ray flux of $\sim 6.4 \times 10^{-8}$ erg s^{-1} cm^{-2} during the transition from HIMS to SIMS. In the early phase of the outburst, type-C QPOs were detected during the HIMS, with centroid frequencies ($\nu_{\rm QPO}$) increasing from ~ 0.11 Hz to 2.3 Hz and corresponding fractional rms amplitudes rising from $\sim 4\%$ to 14%. As the source was transited from HIMS to SIMS, the type-C QPOs disappeared, and a type-B QPO emerged with $\nu_{\rm QPO} \sim 6.4$ Hz and rms amplitude of $\sim 4\%$ during the SIMS.

We have analyzed 2018 outburst of MAXI J1535−571 using *Insight/HXMT* data. The source exhibits type-C QPOs during HIMS where $\nu_{\rm QPO}$ increases from ~ 2.1 Hz to 8.9 Hz and rms$_{\rm QPO}$% decreases from 5.8% to 3.2%. Type-A QPO is observed in the SIMS at $\nu_{\rm QPO} \sim 6.3$ Hz and with rms$_{\rm QPO} \sim 0.99\%$ before the radio flare.

Swift J1658.2−4242 exhibits type-C QPOs with centroid frequencies ranging from ~ 1.5 to 6.6 Hz during the rising phase of the outburst. Near the peak of the outburst, a type-A QPO is detected at $\nu_{\rm QPO} \sim 6-7$ Hz with a fractional rms amplitude of $\sim 2-5\%$. Additionally, a type-B QPO is observed at $\nu_{\rm QPO} \sim 4$ Hz, exhibiting a higher fractional rms amplitude of $\sim 6-8\%$.

4.3 Dependence of Source Inclination on Spectro-Temporal Properties

In the previous section, we study the evolution of spectro-temporal properties of thirteen outbursting BH sources under consideration. Among them, five are low-inclination systems (GX 339−4, 4U 1543−47, XTE J1752−223, XTE J1650−500, Swift J1753.5−0127), while the remaining eight are high-inclination systems (XTE J1859+226, H1743−322, XTE

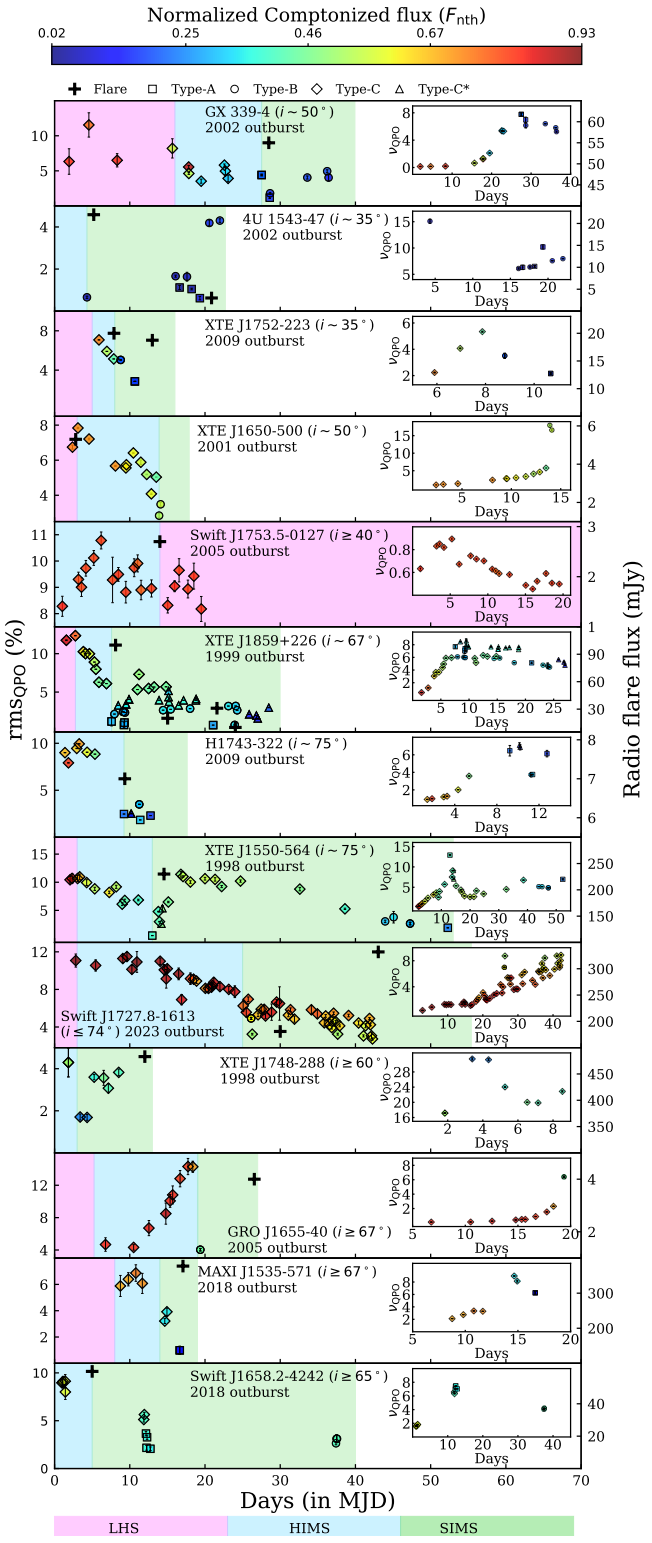

Figure 6. Evolution of QPO rms (rms$_{QPO}$%) with time in GX 339 − 4 ($i \sim 50°$), 4U 1543 − 47 ($i \sim 36°$), XTE J1752 − 223 ($i \sim 35°$), XTE J1650 − 500 ($i \geq 47°$), Swift J1753.5 − 0127 ($i \geq 40°$), XTE J1859 + 226 ($i \sim 65°$), H1743 − 322 ($i \sim 75°$), XTE J1550−564 ($i \sim 74°$), Swift J1727.8−1613 ($i \leq 74°$), XTE J1748−288 ($i \geq 60°$), GRO J1655 − 40 ($i \geq 67°$), MAXI J1535 − 571 ($i \geq 67°$) and Swift J1658.2 − 4242 ($i \geq 65°$). Colorbar represents the normalized Comptonised flux (F_{nth}). Square, circle, diamond and triangle denote different QPO types, and radio flux is indicated using plus symbol. Variation of ν_{QPO} with days are shown in the inset. The presence of radio flux is indicated using plus symbol. For each sources, the duration of the various spectral states are indicated using different shades. See the text for details.

J1550−564, Swift J1727.8−1613, XTE J1748 − 288, GRO J1655−564, MAXI J1535−571 and Swift J1658.2−4242). For these sources, we examine the correlation of spectro-temporal properties (*i.e.*, rms$_{QPO}$%, normalized Comptonized flux F_{nth}, time lag and energy dependent time lag) during the radio flares including spectral state transitions. Subsequently, we put efforts to decode the imprint of inherent coupling between corona and jets for these sources with varied inclination angles ($\sim 35° - 75°$).

In Fig. 6, we illustrate the evolution of rms$_{QPO}$% as well as ν_{QPO} (see the insets) with time during the rising phase of the outburst, highlighting different spectral states — LHS, HIMS, and SIMS — denoted by different shaded regions in the respective panels. The corresponding normalized Comptonized flux (F_{nth}) variations for each source are shown using different colors, where F_{nth} lies in the range $\sim 0.02 - 0.93$ as indicated by the colorbar at the top of the figure. For low-inclination sources, type-A and/or type-B QPOs are generally observed during the radio flares particularly when source transits from HIMS to SIMS, except for Swift J1753.5−0127, where the source transits from HIMS to LHS exhibiting only type-C QPOs during the decay phase of the outburst. Similarly, for high-inclination sources, radio flares are observed during the transition from HIMS to SIMS with the clear presence of type-A and/or type-B QPOs. Moreover, absence of QPO is also occasionally observed after the radio flare in SIMS (see Fig. 6). We further notice that type-A and/or type-B QPOs are often observed during the SIMS with relatively lower Comptonized flux values for majority of the sources except for sources, namely XTE J1550−564, Swift J1727.8−1613, XTE J1859+226 and H1743−322 (2003 outburst), where type-C QPOs are also detected. We observe that rms$_{QPO}$% and F_{nth} are significantly higher for type-C QPOs (usually observed in LHS and HIMS) compared to type-A and type-B QPOs. Near the radio flare, both rms$_{QPO}$% and F_{nth} associated with type-A and type-B are decreased. In fact, for all sources, rms$_{QPO}$% for type-C QPOs increases with F_{nth} indicating that type-C QPOs possibly originate from the Comptonized corona.

In Fig. 7, we examine the possible correlation between F_{nth} and the time lag for type-A, type-B, type-C, and type-C* QPOs across all BH-XRBs under consideration. All together, we have identified 26 type-A, 54 type-B, 199 type-C and 21 type-C* QPOs (see Table 1). The obtained results for low-inclination and high-inclination sources are presented in upper and lower panels, respectively. For low-inclination sources, type-B and type-C QPOs show positive time lags, while type-A QPOs exhibit negative time lags except for one outlier observed during 2002 outburst of GX 339−4. In general, a positive correlation seems to exist between F_{nth} and time lag regardless of the type of QPOs, except for Swift J1753.5−0127. For high-inclination sources, type-A, type-C and type-C* QPOs generally exhibit negative time lags, except XTE J1550 − 564, Swift J1727.8 − 1613, 2003 outburst of H1743 − 322 and GRO J1655 − 40, where both positive and negative lags are observed in type-C QPOs. Type-B QPOs demonstrate both positive and negative lag in high inclination sources. In certain high inclination sources such as XTE J1859 + 226, XTE J1550 − 564 and H1743 − 322, we notice that some type-C QPOs with higher F_{nth} show relatively smaller negative time lags compared to few type-C* and type-A QPOs. As the sources move toward SIMS from HIMS (demarcated by vertical cyan line), they show a shift to negative

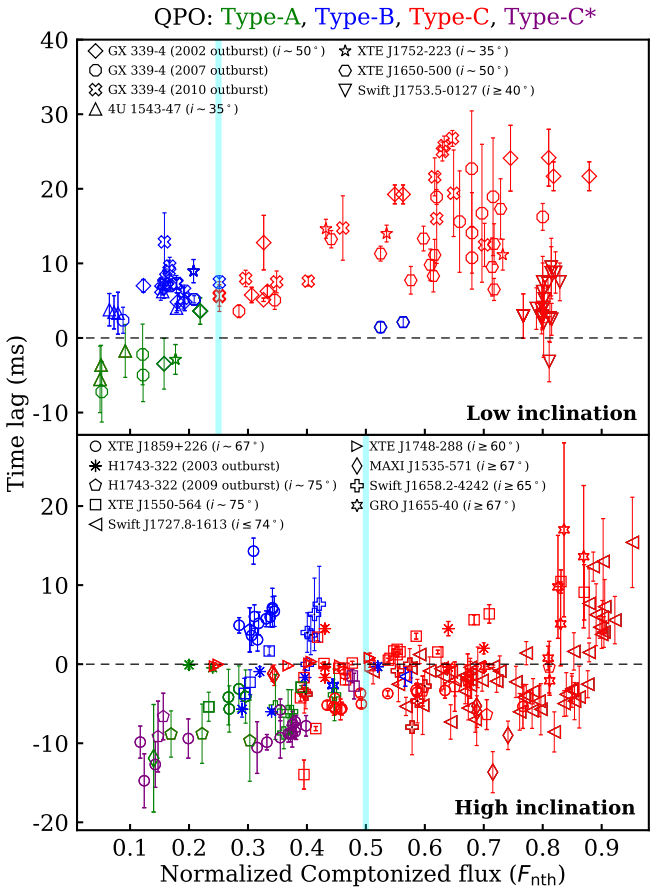

Figure 7. Variation of time lag with F_{nth} for (*upper panel*) low inclination sources (GX 339 − 4, 2002 outburst: Diamond, 2007 outburst: octagon, 2010 outburst: Cross, 4U 1743 − 47: Triangle, XTE J1752 − 223: Asterisk, XTE J1650 − 500: Hexagon, Swift J1753.5 − 0127: Inverted Triangle) and (*lower panel*) high inclination sources (XTE J1859 + 226: Circle, H1743 − 322: Eight pointed asterisk (2003 outburst) and Pentagon (2009 outburst), XTE J1550 − 564: Square, Swift J1727.8 − 1613: Left-caret, XTE J1748−288: Right-caret, MAXI J1535−571: Small Diamond, Swift J1658.2 − 4242: Plus and GRO J1655 − 40: Six pointed star). Vertical line (cyan) separates HIMS and SIMS in both the panels. Green, blue, red and purple colors represent type-A, type-B, type-C and type-C* QPOs. See the text for details.

time lags, accompanied by a decrease in F_{nth}. Note that type-B QPOs generally show positive time lag (2 − 12 ms) with relatively smaller F_{nth} ($\lesssim 0.4$) regardless of the inclination angle of the sources under consideration except H1743 − 322 (2003 outburst), XTE J1550−564, GRO J1655−40 and Swift J1727.8 − 1613. We discuss the implications of these findings for examining different disc configurations in §6.

The evolution of time lag as a function of energy for all BH-XRBs is shown in Fig. 8, with a particular focus on QPOs observed during radio flares, as well as additional detection of type-A and type-B QPOs (see Table 1). Square (green), circle (blue), diamond (red) and triangle (purple) denote type-A, type-B, type-C and type-C* QPOs, respectively. We find that type-C QPOs are observed across all energy bands. For low-inclination sources, type-B and type-C QPOs exhibit positive time lags that increase with energy. Type-A QPOs are observed up to 15 keV in XTE J1752 − 223, 4U 1543 − 47

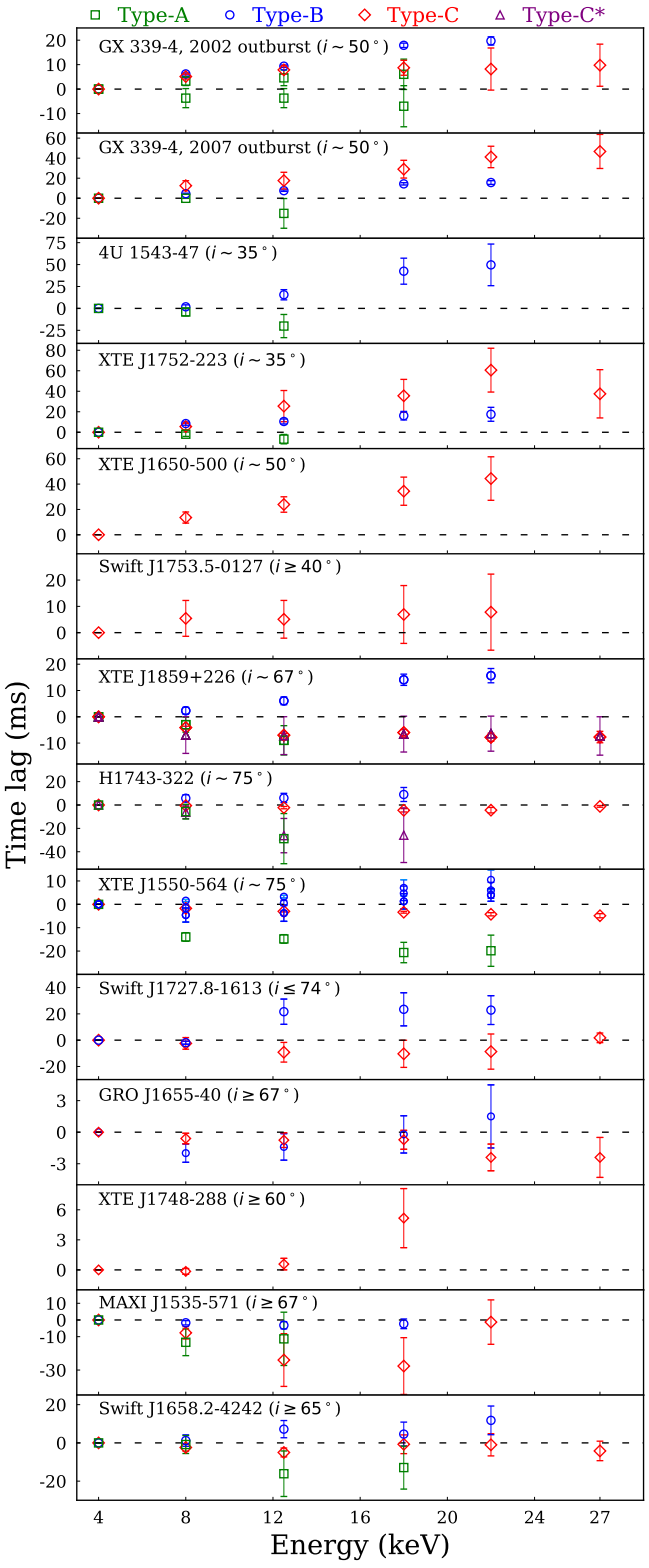

Figure 8. Evolution of time lag with energy in GX 339−4 ($i \sim 50°$), 2002 and 2007 outburst, 4U 1543−47 ($i \sim 36°$), XTE J1752−223 ($i \sim 35°$), XTE J1650 − 500 ($i \geq 47°$), Swift J1753.5 − 0127 ($i \geq 40°$), XTE J1859+226 ($i \sim 65°$), H1743−322 ($i \sim 75°$), XTE J1550 − 564 ($i \sim 74°$) and Swift J1727.8 − 1613 ($i \leq 74°$), GRO J1655−40 ($i \geq 74°$), XTE J1748−288 ($i \geq 60°$), MAXI J1535−571 ($i \geq 67°$), Swift J1658.2 − 4242 ($i \geq 65°$). Different QPOs are represented by different colored symbols (green square: type-A, blue circle: type-B, red diamond: type-C and purple triangle: type-C*). See the text for details.

Table 1. Number of type-C, type-B, type-A, and type-C* QPOs identified at the onset of outbursts in the BH-XRBs under consideration.

Source	Outburst (Year)	Number of QPOs Type-C	Type-B	Type-A	Type-C*
GX 339 − 4	2002	10	5	2	-
	2007	10	3	3	-
	2010	13	12	-	-
4U 1543 − 47	2004	-	5	3	-
XTE J1752 − 223	2009	3	1	1	-
XTE J1650 − 500	2001	11	2	-	-
Swift J1753.5 − 0127	2005	20	-	-	-
XTE J1859 + 226	1999	14	11	4	17
H1743 − 322	2003	4	5	2	-
	2009	6	2	3	2
XTE J1550 − 564	1998	23	3	2	2
Swift J1727.8 − 1613	2023	56	1	-	-
GRO J1655 − 40	2005	9	1	-	-
XTE J1748 − 288	1998	7	-	-	-
MAXI J1535 − 571	2018	6	-	1	-
Swift J1658.2 − 4242	2018	7	3	5	-

and GX 339 − 4 (2007 outburst), and up to 20 keV in 2002 outburst of GX 339 − 4. During the 2002 outburst of GX 339 − 4, the positive time lag and the negative lag associated with type-A QPOs exhibit minimal variation across different energy bands. In high-inclination sources, time lags associated with type-C QPOs show minimal variation with energy. Type-A QPOs are detected up to 10 − 15 keV and generally exhibit little change in time lag across energies, with the exception of XTE J1550−564, which displays a pronounced increase in negative lag with energy.

Since type-B QPOs often correlate with radio flares, we investigate the relationship between the time lags of type-B QPOs and both radio and X-ray fluxes. Fig. 9 presents the variation of time lag with radio flux in panel (a) for low-inclination sources and in panel (b) for high-inclination sources. Panels (c) and (d) display the correlation between time lag and X-ray flux for low- and high-inclination sources, respectively. We normalized the radio flux values to 5 GHz. In low-inclination sources, we find a strong anti-correlation between time lag and radio flux, with a Pearson correlation coefficient ~ -0.93. We also identify a weak anti-correlation between time lag and X-ray flux, with a Pearson correlation coefficient ~ -0.41. In high-inclination sources, we observe a moderate anti-correlation between radio flux and time lag, yielding a Pearson correlation coefficient ~ -0.56 after excluding the source GRO J1655−40. Furthermore, we detect a strong anti-correlation between X-ray flux and time lag, with a Pearson correlation coefficient ~ -0.81, again excluding GRO J1655 − 40. We also mention that for XTE J1752−223, flare F1 is associated with a type-B QPO, while a type-A QPO is detected prior to flare F2. No QPOs are observed in association with the remaining flares.

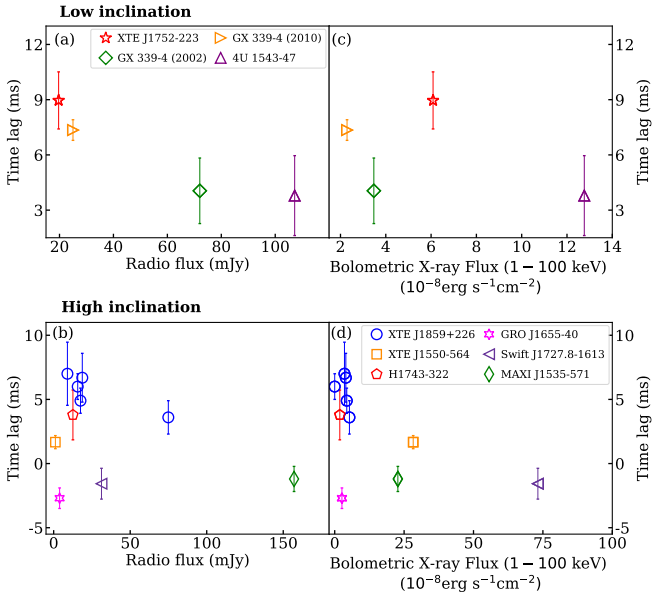

Figure 9. The figure presents the variation of time lag (in milliseconds) with radio flux (in mJy) (in panel (a) and (b)) and bolometric X-ray flux (in panel (c) and (d)) for different black hole X-ray binaries. Panels (a) and (c) correspond to low-inclination sources (XTE J1752 − 223 (red asterisk), GX 339 − 4, 2002 outburst (green diamond), 2010 outburst (orange right-caret), and 4U 1543 − 47 (purple triangle)), while panels (b) and (d) represent high-inclination sources (XTE J1859 + 226 (blue circle), XTE J1550 − 564 (orange square), H1743 − 322 (red pentagon), GRO J1655 − 40 (magenta six-pointed asterisk), Swift J1727.8 − 1613 (violet left-caret), and MAXI J1535 − 571 (green small-diamond)).

5 ESTIMATION OF SPIN AND JET VELOCITY

So far, we have explored the evolution and correlations of the spectro-temporal properties during radio flares and spectral state transitions for the BH-XRBs under consideration. We observe an increase in X-ray flux along with the appearance of type-A/type-B QPOs or their absence near the radio flares across all the sources. In this section, we aim to estimate the jet velocity during the radio flares (*i.e.*, transient jets) in SIMS. To do so, we first calculate the mass accretion rate, which is influenced by radiative efficiency — a factor directly tied to the spin of the sources. In the next sub-section, we present the spin estimates derived using the continuum-fitting method for nine sources, while for the remaining four, we rely on previously reported spin values, as the continuum-fitting method could not be applied (see Section 3.2).

5.1 Estimation of Spin

We constrain the spin ($a_{\rm k}$) of nine BH-XRBs by fixing their mass ($M_{\rm BH}$), inclination (i), and distance (D) as described in Section 3.2. For each source, we select three observations that meet the continuum fitting conditions, namely, f_scat $< 25\%$ and $L_{\rm bol}/L_{\rm Edd} < 0.3$ (Steiner et al. 2011), where $L_{\rm Edd}$ represents the Eddington luminosity and $L_{\rm bol}$ refers to the bolometric luminosity. The estimated spin ($a_{\rm k}$) and accretion rate ($\dot{M}$) of each source is presented in Table 2. It is worth mentioning that the estimated $a_{\rm k}$ values for all sources are consistent with their previous estimates (see references in Table 2). Moreover, a good agreement is observed for the mass accretion rate $\dot{M}$ as obtained using model combination `tbabs`×(`thcomp`⊗`diskbb`). For Swift J1753.5−0127 and Swift J1727.8−1613, the spin values ($a_{\rm k}$) are constrained using reflection modelling as $0.989^{+0.007}_{-0.035}$ (Draghis et al. 2024) and $0.98^{+0.02}_{-0.07}$ (Peng et al. 2024), respectively. For MAXI J1535−571 and Swift J1658.2−4242, spin values were adopted from the literature. The continuum-fitting method could not be applied to Swift J1658.2−4242, as it was not observed in the HSS. In the case of MAXI J1535−571, reliable spin estimation was not possible due to the poor quality of low-energy data (Chen et al. 2020). Subsequently, we calculate the radiative efficiency of accretion disc (η_{acc}) using source spin values $a_{\rm k}$ following Thorne (1974); Hobson et al. (2006) and present in Table 2.

5.2 Estimation of Jet Velocity

Following Longair (2011), we estimate the jet velocity by applying minimum energy condition which implies that the minimum energy contained in the blob of ejected plasma is given by,

$$W_{\rm min} = 3 \times 10^{6}\ \eta^{4/7} V^{3/7} \nu^{2/7} S_{\nu}^{4/7} D^{8/7}\ \text{Joule}, \tag{6}$$

where S_ν is the observed radio flux at radio frequency ν, D is the distance of the source and V is the volume of the spherical plasma blob. Here, η denotes the relativistic correction factor assumed to be unity (Brocksopp et al. 2002; Nandi et al. 2018). Considering $V = (\beta c t)^3$, where t is the rise-time of the radio event and β is the jet velocity in the unit of c, the observed jet power is estimated as,

$$L_{\rm jet} = \frac{W_{\rm min}}{t} = 3 \times 10^{33} \left(\frac{S_\nu}{\rm mJy}\right)^{4/7} \left(\frac{D}{\rm kpc}\right)^{8/7} \left(\frac{\nu}{\rm GHz}\right)^{2/7} \left(\frac{t}{\rm s}\right)^{2/7} \beta^{9/7}\ \text{erg s}^{-1}. \tag{7}$$

We use equation (1) to normalize the radio flux at frequency $\nu = 5$ GHz. Following Fender (2001b); Miller-Jones et al. (2006), we apply Doppler correction and obtain the intrinsic radio flux ($S_\nu^{\rm int}$) using observed radio flux (S_ν) as $S_\nu^{\rm int} = \delta^{\alpha-k} S_\nu$, where $\nu = \delta \times \nu^{\rm int}$, $\delta^{-1} = \gamma(1 - \beta \cos i)$, δ being the Doppler factor and γ ($= 1/\sqrt{1-\beta^2}$) is the Lorentz factor. We assume the radio flux to follow a power law $S_\nu = \nu^\alpha$, where t transforms as $t = t^{\rm int}/\delta$ for simplicity. The parameter k accounts for the characteristics of the ejecta, where $k = 2$ and $k = 3$ refer steady continuous jet and discrete jet, respectively (Rybicki & Lightman 1979). With this, the intrinsic jet power is calculated as,

$$L_{\rm jet}^{\rm int} = \delta^{4(\alpha-k)/7} \times L_{\rm jet} = [\gamma(1 - \beta \cos i)]^{4(k-\alpha)/7} \times L_{\rm jet}. \tag{8}$$

During accretion, a part of the inflowing matter may deflect along the rotation axis of the black hole producing bipolar jets. For a given mass accretion rate ($\dot{M}$), we compute the jet kinetic power as,

$$L_{\rm jet}^{\rm est} = \frac{1}{2}\ \eta_{\rm jet} \times \varepsilon \times \dot{M} \times c^2, \tag{9}$$

where $\eta_{\rm jet}$ is the jet radiative efficiency factor assumed as ~ 0.1 (Fender 2001a) and ε accounts the fraction of energy transferred to jets from the disc (Chakrabarti 1999; Das et al. 2001; Aktar et al. 2019).

Given the unabsorbed X-ray flux ($F_{\rm x}$) of a source with distance D, the accretion rate can be calculated using the X-ray luminosity $L_{\rm x}$ ($= 4\pi D^2 F_{\rm x}$) as,

$$\dot{M} = 8.73 \times 10^{-17} \times \eta_{\rm acc} \left(\frac{F_{\rm x} D^2}{c^2}\right) \left(\frac{M_{\rm BH}}{M_\odot}\right)^{-1} \dot{M}_{\rm Edd}, \tag{10}$$

where $\dot{M}_{\rm Edd} = 1.47 \times 10^{18}\ (M_{\rm BH}/M_\odot)$ g s^{-1}. In this study, we focus on observations taken at the peak bolometric X-ray flux or during type-A/type-B QPOs in SIMS, particularly around the radio flares, while for HIMS, the X-ray flux is determined using the closest available X-ray observation relative to the radio flare. The rise time t is estimated as the interval between the X-ray observation used to calculate $\dot{M}$ and the observation with radio flare. Using equation (7) in equation (8) and then equating with equation (9), we estimate the jet velocity β in unit of c. Following Fender et al. (2004, 2009), we adopt $k = 2$ during the HIMS for continuous jets, and $k = 3$ during the SIMS, when jets are discrete.

In Fig. 10, we depict the variation of jet velocity (β) with ε for BH-XRBs under consideration. Panel (a) shows the results for sources with low-inclination, including GX 339−4 (2002 and 2010 outbursts), 4U 1543−47, XTE J1752−223, XTE J1650−500, and Swift J1753.5−0127. Panel (b) displays the results for sources with high-inclination, such as XTE J1859+226, MAXI J1535−571, H1743−322, (2003 and 2009 outbursts), XTE J1550−564, Swift J1727.8−0127 and GRO J1655−40. The shaded regions denote the range of velocities resulting due to the uncertainty in estimating $\eta_{\rm acc}$ that largely depends on the black hole spin ($a_{\rm k}$) estimate (see Table 2). Note that jet velocity couldn't be reliably estimated for Swift

Table 2. Fitted parameters using model `kerrbb2` with 90% confidence in GX 339 − 4, 4U 1543 − 47, XTE J1752 − 223, XTE J1650 − 500, XTE J1859 + 226, H1743 − 322, XTE J1550 − 564 and GRO J1655 − 40, XTE J1748 − 288 and their corresponding radiative efficiency of the accretion disc η_{acc}. For Swift J1753.5 − 0127, Swift J1727.8 − 1613, Swift J1658.2 − 4242 and MAXI J1535 − 571, the continuum fitting method cannot be applied, and the spin values are taken from the literature.

Source	Date (MJD)	D (kpc)	i (°)	$M_{\rm BH}$ ($M_\odot$)	a_k	$\dot{M}^{\boxplus}_{acc}$ ($\dot{M}_{Edd}$)	η_{acc}	References
GX 339 − 4	52660.64	8.4	50	9.4	0.53 ± 0.02	$0.12^{\dagger}$	0.08 − 0.09	[1], [2], [3], [4], [5]
	52667.02				$0.60^{+0.03}_{-0.05}$	$0.11^{+0.01}_{-0.01}$		
	52671.25				0.58 ± 0.03	0.10 ± 0.01		
4U 1543 − 47	52468.72	7.5	35	9.4	0.44 ± 0.05	0.16 ± 0.01	0.07 − 0.09	[6], [7]
	52469.23				$0.43^{+0.06}_{-0.05}$	0.16 ± 0.01		
	52473.17				$0.52^{+0.06}_{-0.08}$	0.10 ± 0.01		
XTE J1752 − 223	55252.59	7.1	35	12	$0.52^{+0.07}_{-0.09}$	$0.08^{\dagger}$	0.07 − 0.10	[8], [9], [10], [11], [12]
	55256.74				$0.62^{+0.02}_{-0.06}$	0.06 ± 0.01		
	55260.80				$0.46^{+0.11}_{-0.09}$	0.08 ± 0.01		
XTE J1650 − 500	52174.29	2.6	50	5.1	$0.63^{+0.06}_{-0.07}$	$0.10^{\dagger}$	0.09 − 0.11	[13], [14], [15], [16]
	52217.47				0.65 ± 0.05	$0.03^{\dagger}$		
	52352.65				$0.62^{+0.10}_{-0.07}$	0.04 ± 0.01		
XTE J1859 + 226	51502.25	6	67	7.8	$0.34^{+0.03}_{-0.04}$	0.13 ± 0.01	0.07 − 0.08	[12], [17], [18], [19], [20]
	51504.32				$0.32^{+0.05}_{-0.04}$	0.13 ± 0.01		
	51520.08				$0.34^{+0.07}_{-0.06}$	0.10 ± 0.01		
H1743 − 322	54997.26	8.5	75	11.2	$0.36^{+0.05}_{-0.06}$	0.17 ± 0.01	0.07 − 0.08	[21], [22]
	54999.74				$0.43^{+0.06}_{-0.09}$	0.14 ± 0.01		
	55220.36				$0.39^{+0.14}_{-0.15}$	0.13 ± 0.03		
XTE J1550 − 564	51266.87	4.4	75	9.1	$0.35^{0.05}_{0.03}$	0.16 ± 0.01	0.07 − 0.08	[23], [24], [25]
	51270.74				$0.38^{+0.03}_{-0.05}$	0.10 ± 0.01		
	51274.47				$0.42^{+0.03}_{-0.05}$	0.10 ± 0.01		
GRO J1655 − 40	53449.84	3.2	65	6.0	$0.82^{+0.010}_{-0.003}$	0.12 ± 0.01	0.11 − 0.13	[26], [27], [28], [29], [30]
	53616.79				0.78 ± 0.01	0.04 ± 0.01		
	53619.87				$0.76^{+0.01}_{-0.04}$	0.04 ± 0.01		
XTE J1748 − 288	50986.93	8.7	65	7.6	0.80 ± 0.01	0.23 ± 0.01	0.12 − 0.13	[12], [31]
	50991.48				0.81 ± 0.01	0.09 ± 0.01		
	50996.75				0.83 ± 0.02	0.07 ± 0.01		
Swift J1753.5 − 0127	-	7.1	≥ 40	7.4	$0.989^{+0.007}_{-0.035}$	-	0.19 − 0.29	[32], [33], [34], [35]
Swift J1727.8 − 1613	-	3.7	≤ 74	3.1	$0.98^{+0.02}_{-0.07}$	-	0.16 − 0.30	[36], [37], [38], [39]
MAXI J1535 − 571	-	3.7	≥ 67	3.1	0.992 ± 0.001	-	0.26 − 0.28	[40], [41], [42], [43], [44]
Swift J1658.2 − 4242	-	6.3	≥ 65	14	≥ 0.96	-	≥ 0.20	[45], [46]

$^{\boxplus}\dot{M}_{Edd} = 1.47 \times 10^{18}\ M_{\rm BH}/M_\odot$ erg s^{-1}.†Error is insignificant upto two decimal places.

Reference: [1] Heida et al. (2017), [2] Fürst et al. (2015), [3] Parker et al. (2016), [4] Zdziarski et al. (2019), [5] Shidatsu et al. (2011), [6] Dong et al. (2020), [7] Chen & Wang (2024), [8] Miller-Jones et al. (2011), [9] Shaposhnikov et al. (2010), [10] García et al. (2018), [11] Debnath et al. (2021), [12] Abdulghani et al. (2024), [13] Slaný & Stuchlík (2008), [14] Orosz et al. (2004), [15] Homan et al. (2006), [16] Mondal (2009), [17] Hynes et al. (2002), [18] Motta et al. (2022), [19] Corral-Santana et al. (2013), [20] Yanes-Rizo et al. (2022), [21] Steiner et al. (2012), [22] Molla et al. (2017), [23] Jonker et al. (2010), [24] Jonker & Nelemans (2004), [25] Orosz et al. (2011), [26] Ponti et al. (2012), [27] Shafee et al. (2006), [28] Greene et al. (2001), [29] Kuulkers et al. (2000), [30] Hjellming & Rupen (1995), [31] van den Eijnden et al. (2017), [32] Shaw et al. (2016), [33] Gandhi et al. (2019), [34] Neustroev et al. (2014), [35] Draghis et al. (2024), [36] Mata Sanchez et al. (2024), [37] Peng et al. (2024), [38] Wood et al. (2024), [39] Yu et al. (2024), [40] Sreehari et al. (2019), [41] Sridhar et al. (2019), [42] Liu et al. (2022), [43] Chauhan et al. (2019), [44] Miller et al. (2018), [45] Xu et al. (2018), [46] Mondal & Jithesh (2023).

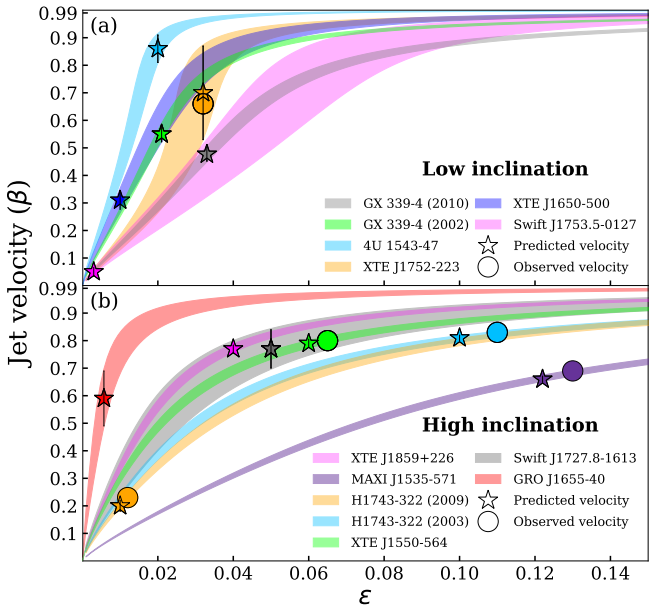

Figure 10. Variation of jet velocity (shaded region) with ε (accounts the fraction of energy transferred to jets from disc) for (a) low-inclination sources such as, GX 339−4 (green for 2002 outburst and grey for 2010 outburst), 4U 1543 − 47 (skyblue), XTE J1752 − 223 (orange), XTE J1650 − 500 (blue), Swift J1753.5 − 0127 (pink) and (b) high-inclination sources such as, XTE J1859 + 226 (pink), MAXI J1535 − 571 (violet), H1743 − 322, 2009 outburst (orange), H1743 − 322, 2003 outburst (skyblue), XTE J1550 − 564 (green), Swift J1727.8 − 0127 (grey), GRO J1655 − 40 (red). The values of radiative efficiency of disc $\eta_{\rm acc}$ are taken from Table 1. Asterisks represent the jet velocity β predicted from our calculations and circles represent the velocity reported earlier.

J1658.2−4242 and XTE J1748−288 due to large uncertainties arising from the observational gap between X-ray and radio data. The radiative efficiency of the disc is expressed $\eta_{\rm acc} = 1 - \mathcal{E}_{\rm ISCO}$ (Thorne 1974; Hobson et al. 2006; Shapiro & Teukolsky 1983), where the specific energy ($\mathcal{E}_{\rm ISCO}$) at the innermost stable circular orbit ($R_{\rm ISCO}$) is given by, $\mathcal{E}_{\rm ISCO} = \left(1 - \frac{2M}{R_{\rm ISCO}} \pm a_k\sqrt{\frac{M}{R^3_{\rm ISCO}}}\right)\left(1 - \frac{3M}{R_{\rm ISCO}} \pm 2a_k\sqrt{\frac{M}{R^2_{\rm ISCO}}}\right)^{-1/2}$. For a Kerr black hole, $R_{\rm ISCO}$ is expressed as (Bardeen et al. 1972; Shakura & Sunyaev 1973), $R_{\rm ISCO} = M\left(3 + Z_2 \mp \sqrt{(3 - Z_1)(3 + Z_1 + 2Z_2)}\right)$, where $Z_1 = 1 + \left(1 - (a_k/M)^2\right)^{1/3}\left[(1 + a_k/M)^{1/3} + (1 - a_k/M)^{1/3}\right]$, $Z_2 = \sqrt{3(a_k/M)^2 + Z_1^2}$ and M is the mass of the black hole. Here, the negative sign corresponds to prograde orbits, while the positive sign applies to retrograde orbits. We observe that β increases with ε for all sources. For a given ε, β has both upper and lower limits: the upper limit corresponds to the minimum estimate of a_k, while the lower limit corresponds to the maximum estimate of a_k. These findings suggest that the impact of black hole spin a_k on determining the jet velocity β appears to be minimal.

Meanwhile, the jet velocity during the radio flare has been reported for few sources. For H1743 − 322, the jet velocities during the 2003 and 2009 outbursts were measured as $\beta \sim 0.8$ and $\beta \sim 0.2$, respectively, based on the proper motion of the jet ejecta (Corbel et al. 2005; Miller-Jones et al. 2012). Using these, we estimate $\varepsilon \sim 0.10$ for 2003 outburst and 0.01 for 2009 outburst. For the 1998 outburst of XTE J1550−564, Hannikainen et al. (2009) reported the jet velocity $\beta \geq 0.8$ that holds for $\varepsilon \geq 0.06$. For MAXI J1535 − 571, β is reported as ~ 0.69 (Russell et al. 2019), that corresponds to $\varepsilon \geq 0.12$. In the case of F4 in XTE J1752 − 223, the jet velocity was estimated as $\beta \geq 0.66$ (Miller-Jones et al. 2011) yielding $\varepsilon \sim 0.03$. The open circles in Fig. 10 represent the observed values of β. These findings clearly indicate that the observed β is resulted from approximately 1 − 12% of the accreting matter being ejected from the disc as jets in BH-XRBs. For these sources, the predicted values of ε are in good agreement with the difference between the normalized Comptonized fluxes ($F_{\rm nth}$) of successive observations during radio flares. Considering this, we estimate the efficiency ε during the radio flares and predict the jet velocity β for the remaining sources, which are marked using asterisk in Fig. 10 for each sources, and the results are summarized in Table 3.

Since the observed radio luminosity $L_{\rm R}$ ($= \nu S_\nu D^2$) is likely to be influenced by Doppler boosting, we investigate the relationship between $L_{\rm R}$ and the intrinsic radio luminosity $L_{\rm R}^{\rm int}$ ($= \delta^{\alpha-k-1} L_{\rm R}$) to assess the impact of Doppler correction on the measured values. In Fig. 11, we present the variations

Table 3. Estimated jet velocities (β) during radio flares in the BH-XRBs under consideration. For sources exhibiting multiple radio flares, the resulting β values vary accordingly.

Source	Date†		ε	β
	Before flare	After flare		
GX 339 − 4	52406.0	52408.0	0.021	0.52 − 0.58
GX 339 − 4	55310.0	55314.1	0.033	0.45 − 0.50
4U 1743 − 47	52443.2	52445.5	0.02	0.81 − 0.91
XTE J1752 − 223 (F1)	55218.1	55218.8	0.061	0.96 − 0.98
XTE J1752 − 223 (F2)	55220.37	55222.92	0.061	0.37 − 0.75
XTE J1752 − 223 (F3)	55221.08	55223.86	0.007	0.33 − 0.61
XTE J1752 − 223 (F4)	55231.61	55238.93	0.032	0.53 − 0.87
XTE J1752 − 223 (F5)	55249.65	55250.00	0.012	0.26 − 0.42
XTE J1752 − 223 (F6)	55258.71	55260.83	0.005	0.13 − 0.17
XTE J1752 − 223 (F7)	55278.58	55278.96	0.005	0.14 − 0.18
XTE J1650 − 500	52160.4	52161.1	0.012	0.23 − 0.34
Swift J1753.5 − 0127	53560.5	53567.0	0.003	0.03 − 0.06
XTE J1859 + 226 (HIMS)	51464.1	51464.6	0.002	0.08 − 0.09
XTE J1859 + 226 (F1)	51467.9	51468.5	0.040	0.75 − 0.78
XTE J1859 + 226 (F2)	51474.3	51474.8	0.030	0.72 − 0.76
XTE J1859 + 226 (F3)	51477.1	51478.8	0.030	0.65 − 0.69
XTE J1859 + 226 (F4)	51483.9	51484.07	0.020	0.65 − 0.69
H1743 − 322 (2009)	54987.2	54989.1	0.010	0.18 − 0.22
H1743 − 322 (2003)	52735.7	52737.5	0.100	0.80 − 0.82
XTE J1550 − 564	51075.9	51078.1	0.061	0.78 − 0.81
Swift J1727.8 − 1613	60206.1	60211.1	0.050	0.70 − 0.84
Swift J1727.8 − 1613	60221.8	60222.1	0.020	0.55 − 0.73
GRO J1655 − 40	53446.89	53448.01	0.006	0.49 − 0.69
MAXI J1535 − 571	58019.1	58019.9	0.122	0.65 − 0.67

†Successive X-ray observations during radio flare are used to estimate ε.

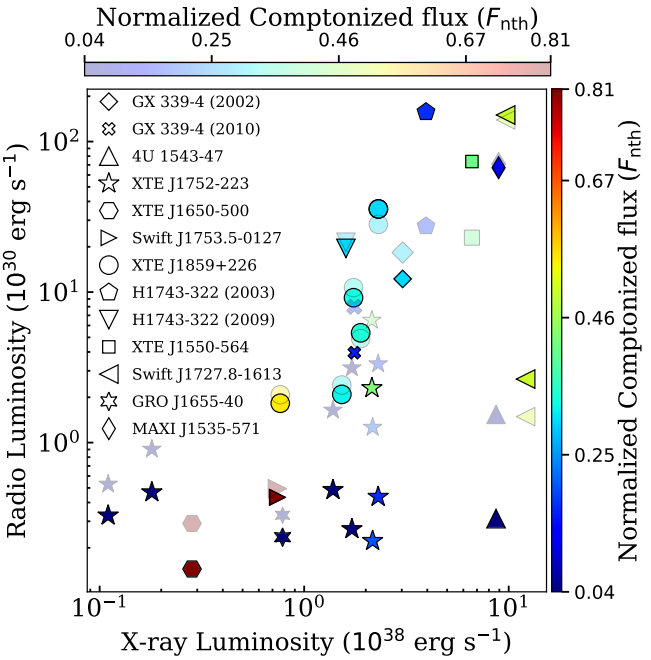

Figure 11. Variation of intrinsic radio luminosity $L_{\rm R}^{\rm int}$ (opaque) and $L_{\rm R}$ (semi-transparent) observed radio luminosity with X-ray luminosity for GX 339−4 (2002 and 2010 outbursts denoted with diamond and cross), 4U 1543−47 (triangle), XTE J1752−223 (asterisk), XTE J1650−500 (hexagon), Swift J1753.5−0127 (right-caret), XTE J1859+226 (circle), H1743−322 (2003 and 2009 outbursts are shown with pentagon and inverted triangle), XTE J1550−564 (square), Swift J1727.8−1613 (left-caret), GRO J1655 − 40 (six-pointed stars) and MAXI J1535 − 571 (small diamond). Colorbars at the top and right of the figure denote the range of $F_{\rm nth}$ obtained from spectral modelling. See the text for details.

of $L_{\rm R}$ and $L_{\rm R}^{\rm int}$ with X-ray luminosity ($L_{\rm bol}$). Results obtained for different sources are represented by distinct symbols: GX 339−4 (2002 and 2010 outbursts are denoted with diamond and cross), 4U 1543−47 (triangle), XTE J1752−223 (asterisk), XTE J1650−500 (hexagon), Swift J1753.5−0127 (right-caret), XTE J1859+226 (circle), H1743−322 (2003 and 2009 outbursts are shown with pentagon and inverted triangle), XTE J1550−564 (square), Swift J1727.8−1613 (left-caret), GRO J1655 − 40 (six-pointed stars) and MAXI J1535 − 571 (small diamond). Opaque and semi-transparent symbols represent $L_{\rm R}^{\rm int}$ and $L_{\rm R}$, respectively, with colors indicating the range of normalized Comptonized flux ($F_{\rm nth}$), as shown by the colorbar at the top and right of the figure. All sources exhibit a normalized Comptonized flux value of $F_{\rm nth} > 0.5$ in HIMS and $F_{\rm nth} \leq 0.5$ in SIMS. Sources in HIMS show lower radio and X-ray luminosities compared to those in SIMS. The difference between $L_{\rm R}$ and $L_{\rm R}^{\rm int}$ possibly suggests the influence of relativistic beaming on jet emissions. Furthermore, we observe that both $L_{\rm R}$ and $L_{\rm R}^{\rm int}$ increase with the increase of X-ray luminosity. However, in XTE J1752−223, corresponding to F6 and F7, the source is in the soft state, where both X-ray and radio luminosities as well as the normalized Comptonized flux are lower. It is important to note that for low-inclination sources, the observed luminosity ($L_{\rm R}$) tends to be higher than the intrinsic luminosity ($L_{\rm R}^{\rm int}$). This pattern also holds for high-inclination sources when the jet velocity remains in the range $\beta \sim 0.13 - 0.65$. However, for highly inclined sources ($i \gtrsim 60°$) with higher jet velocities, the intrinsic luminosity ($L_{\rm R}^{\rm int}$) exceeds the observed luminosity ($L_{\rm R}$).

6 DISCUSSION AND CONCLUSION

In this work, we perform a comprehensive spectro-temporal analyses of thirteen BH-XRBs during their entire outbursts using *RXTE*, *Insight/HXMT* and *AstroSat* observations. We examine the spectro-temporal properties during the radio flares to investigate the disc-jet connection. Further, we focus on estimating the accretion rate ($\dot{m}$) and black hole spin (a_k), while computing the velocity (β) of the plasma ejected in the form of jets.

6.1 Spectro-temporal Properties to Probe Disc-Jet Connection

The transition from HIMS to SIMS is characterized by an increase in X-ray flux, which coincides with the onset of radio flares, as shown in Fig. 1. This transition is also linked to the appearance of type-A and type-B QPOs near radio flares in both high- and low-inclination sources (see Fig. 2 and Fig. 4). Similar coincidence of X-ray peak and radio flare is also observed in SIMS, both in presence and absence of QPOs (see Fig. 6). In high-inclination sources, such as XTE J1859+226 and H1743−322, type-B QPOs emerge near radio flares, displaying a positive time lag, in contrast to the negative time lag observed with type-C QPOs (see Fig. 7). Similarly, in XTE J1550 − 564, H1743 − 322 (2003 outburst), GRO J1655 − 40 and Swift J1727.8 − 1613, type-A and type-B QPOs are detected near radio flares with negative time lag, while type-C QPOs show positive time lag with relatively higher $F_{\rm nth}$. For low-inclination sources, such as GX 339−4, 4U 1543−47, and XTE J1752−223, type-B QPOs are observed near radio flares with positive time lags, while XTE J1650−500 lacks concurrent radio observations during the occurrence of type-A or type-B QPOs (see Fig. 6). During the failed outburst of Swift J1753.5−0127, only type-C QPOs are detected with positive time lag.

We observe that higher rms$_{\rm QPO}$% in type-C QPOs is correlated with normalized Comptonized flux ($F_{\rm nth}$) in all sources (see Fig. 6). These findings indicate that type-C QPOs are possibly originated from the disc-corona (see also Titarchuk & Fiorito 2004; Ingram et al. 2009; Nandi et al. 2012; Iyer et al. 2015; Motta et al. 2015; Nandi et al. 2024). Meanwhile, the origin of type-B QPOs has also been attributed to the corona (Gao et al. 2014; Motta et al. 2015; García et al. 2021; Belloni et al. 2020; Zhang et al. 2023), although Fender et al. (2009); Radhika & Nandi (2014); Radhika et al. (2016); Harikrishna & Sriram (2022); Zhang et al. (2023) suggest a potential link between type-B QPOs and the radio jets. This emphasizes the crucial role of the corona in driving both QPO variability and jet ejections, and hence, we investigate how the time-lag varies with $F_{\rm nth}$ (see Fig. 7). In low-inclination sources, type-C and type-B QPOs generally show positive lags, whereas type-A QPOs exhibit both positive and negative lags. In high-inclination sources, type-C QPOs display both positive and negative lags depending on the Comptonized emission, while Type-C* and type-A QPOs predominantly exhibit negative lags. Type-B QPOs having similar

$F_{\rm nth}$ as that of type-A QPO shows both positive and negative lag. Our results align with the finding of van den Eijnden et al. (2017) for type-C QPOs and type-A QPOs, which suggests that the time lag of type-C QPOs is influenced by the source inclination, except for Swift J1727.8 − 1613, GRO J1655 − 40, XTE J1550 − 564 and 2003 outburst of H1743 − 322. In contrast, the time lag for type-A QPO appears to be independent of sources inclination. For type-B QPOs, the time lag does show an inclination dependence, particularly low-inclination sources exhibit positive lags, while high-inclination sources display both positive and negative lags.

It is worth mentioning that positive time lags are generally attributed due to the inverse Comptonization of soft photons in the corona (Reig et al. 2000), while negative time lags are associated with multiple physical processes, including Compton down-scattering in the corona (Reig et al. 2000), reprocessing of hard photons in the accretion disc (Uttley et al. 2014; Karpouzas et al. 2020), and gravitational bending (Dutta & Chakrabarti 2016; Chatterjee et al. 2017). Meanwhile, Dutta & Chakrabarti (2016) argued that a larger Comptonizing region reduces QPO frequency, thereby increasing the time lag. The observed rise in positive time lags with increasing Comptonized emissions strongly suggests that the size of the corona significantly influences the time lag characteristics. We find that the positive time lags of type-C QPOs generally increase with energy, while negative time lags show marginal variation (see Fig. 8). The increase in positive time lag with energy suggests that as seed photons are reprocessed for longer time in the corona, emergent radiations gain energy through up-scattering, resulting in longer delays.

Furthermore, for type-C QPOs, up-scattered photons directly reach the observer in low-inclination sources. For high-inclination sources, the initially large corona produces up-scattered X-ray photons through inverse Compton scattering. Most of these up-scattered photons escape without interacting significantly with the disc and leading to positive time lags. As the corona shrinks, a greater fraction of hard photons are redirected back toward the disc, where they interact with the thermalized disc, lose energy, and contribute to the softer X-ray emissions. This reprocessing mechanism eventually gives rise to negative lags. During the LHS and HIMS, the non-thermal flux fraction ($F_{\rm nth}$) is high ($\gtrsim 0.8$), indicating a large coronal size in both low- and high-inclination systems. In low-inclination sources, as the corona begins to shrink during HIMS ($F_{\rm nth} \sim 0.65-0.7$), the lag remains positive. Under similar conditions, however, high-inclination sources begin to show negative lags, suggesting more efficient reprocessing due to the increased interaction between coronal photons and the disc. When $F_{\rm nth}$ decreases further ($\lesssim 0.5$) and the corona becomes more radially compact, both low- and high-inclination sources exhibit negative lags. Interestingly, type-A QPOs are generally associated with minimal hard X-ray emissions compared to other QPOs and show a negative lag, except one observation in 2002 outburst of GX 339−4, suggesting that they originate from a smaller corona. In contrast, type-B QPOs, which appeared with Comptonized emissions similar to type-A QPOs but significantly lower than type-C QPOs, show positive lag for low inclination sources and both positive and negative lags for high inclination sources. With this, we argue that the corona associated with type-B QPOs is likely to differ in geometry from that of type-C QPOs, possibly being vertically elongated as it appears to be connected with radio ejections. This finding also corroborates the previous studies Homan et al. (2020); Belloni et al. (2020); García et al. (2021); Méndez et al. (2022); Ma et al. (2023); Zhang et al. (2023).

The present study indicates that type-A QPOs, which exhibit negative time lags, act as precursors to radio ejections in sources such as XTE J1752−223, XTE J1859+226, H1743−322, XTE J1550−564, and MAXI J1535−571, and may serve as potential indicators of changes in the coronal geometry. Notably, when type-B QPOs are observed with positive lags, a vertically elongated corona emerges leading to jet ejections in the form of radio flares (see also Stevens & Uttley 2016; Belloni et al. 2020; Kylafis et al. 2020; Chatterjee et al. 2020; García et al. 2021; Harikrishna & Sriram 2022; Liu et al. 2022; Méndez et al. 2022; Zhang et al. 2023). In contrast, type-B QPOs exhibiting negative lags are likely produced by a radially compact corona that is in the process of transitioning toward a vertical geometry, which possibly later results in jet ejection. The decrease in time lag of type-B QPOs with increasing radio and X-ray fluxes (Fig. 9) for both low- and high-inclination sources further substantiates the scenario in which the radial extent of the corona diminishes as more coronal mass is redirected vertically, eventually leading to discrete jet ejection. This interpretation is further supported by the consistent disappearance of QPOs following such type-B events, although concurrent radio observations are not always available to confirm jet activity.

6.2 Possible Disc Configurations with Source Inclination

Following the discussions in the previous section, we explore the possible configuration of the disc-jet geometry in the context of time lag behavior and Comptonized emissions for type-A, type-B and type-C QPOs, as shown in Fig. 12. Four different possible disc-jet configurations are identified as delineated below.

- Configuration-I (Large Radially Extended Corona): A large radially extended corona leads to minimal reprocessing of up-scattered photons in the disc for both high and low-inclination sources resulting in positive lags for type-C QPOs with high normalized Comptonized flux.
- Configuration-II (Small Radially Extended Corona): Reduced coronal size increases the possibility of reprocessing of hard photons in the disc causing negative lags in high-inclination sources. The time lags remain positive in low-inclination sources as the effect of reprocessing remains weaker.
- Configuration-III (Radially and Vertically Compact Corona): As the radial extent of the corona shrinks and it begins to elongate vertically, reprocessing of hard photons in the disc increases regardless of the source inclination, resulting in negative lag. The modulation of the radially compact corona gives rise to type-A QPO, which seems to act as precursors to the subsequent jet ejections.
- Configuration-IV (Vertically Elongated Corona or Radially Compact Corona): The vertical elongation of the corona reduces the possibility of interaction between up-scattered photons and the disc, leading to a positive lag of type-B QPOs. This happens irrespective to the source inclinations. The presence of radio flares near type-B QPOs along with the reduced Comptonized X-ray flux further substantiates the

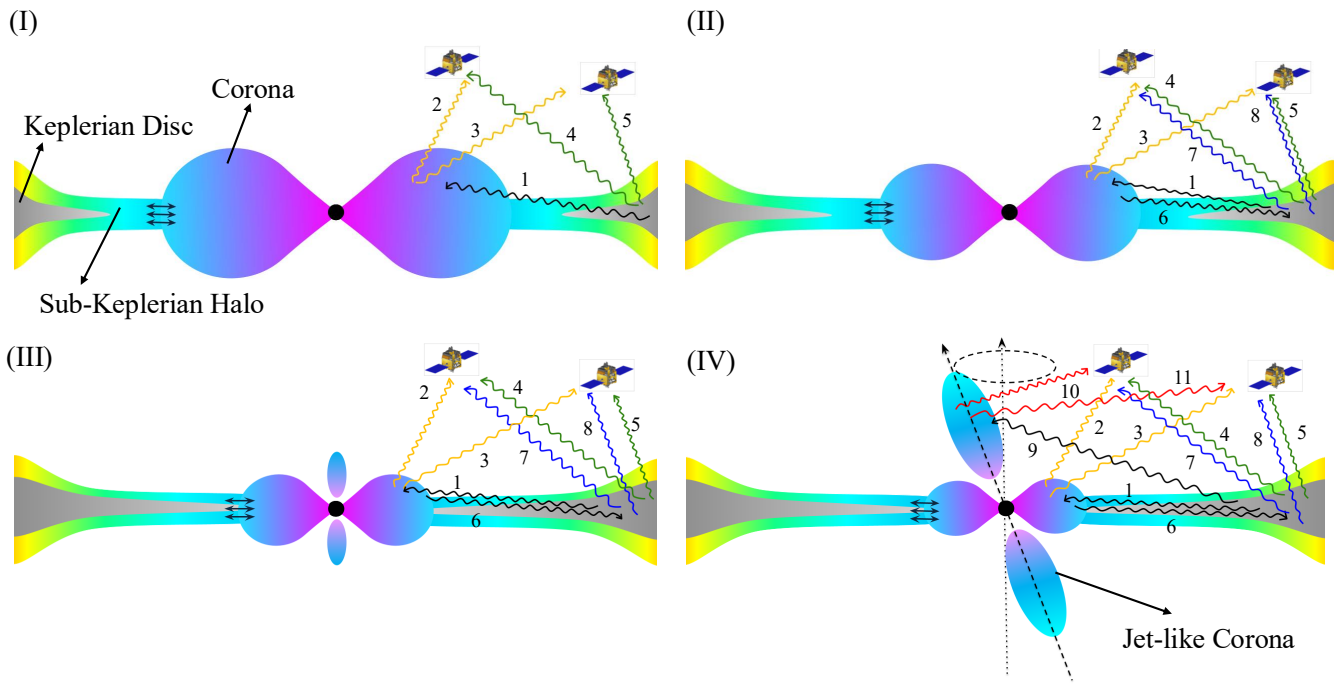

Figure 12. Schematic representation of disc-jet scenarios: (I) Corona is radially extended and large in size, (II) Corona is radially extended but smaller in size, (III) Radial extent of corona is reduced and begins to elongate vertically, and (IV) Radial extent of corona is small and extends vertically. Soft photons reaching the observer directly from the disc are marked in green, while reprocessed photons are shown in blue. Hard photons reaching the observer from the radial corona is marked in yellow. Hard photons originating from the vertical corona, reaching the observer is shown in red. Soft photons incident on the corona from the disc and hard photons from corona to disc are shown in black. In (I), (II), (III) and (IV), the double headed arrows in the radial corona represent the oscillation of the corona causing type-C, type-A and type-B (negative lag) QPOs. In (IV), the dotted line marks the black hole's spin axis, while the dashed line represents the misaligned jet axis, causing the precession. See the text for details.

concept of a vertically extended corona. When such a elongated corona precesses around the black hole's rotation axis, it could modulate the emerging hard radiation, leading to the formation of type-B QPOs. Moreover, in high-inclination sources, type-B QPOs with negative time lags possibly arise when up-scattered photons from the radially compact corona undergo additional reprocessing after interacting with the disc before reaching the observer.

We illustrate all four disc-jet configurations in Fig. 12, where the arrows marked with numbers represent the different photon paths. For example, (1) soft photons from the Keplerian disc incident upon the corona, (2) up-scattered photons reaching the observer at low-inclination, (3) up-scattered photons observed at high-inclination, (4) soft photons from the disc reaching the observer at low-inclination, (5) soft photons reaching the observer at high-inclination, (6) up-scattered photons returning to the disc, (7) reprocessed photons reaching the observer at low-inclination, and (8) reprocessed photons reaching the observer at high-inclination. (9) Soft photons interacting with the vertically extended corona, (10) up-scattered photons reaching a low-inclination observer from the vertically elongated corona, and (11) up-scattered photons reaching a high-inclination observer from the same vertically elongated corona. To distinguish between reprocessed soft photons and direct photons from the disc, we denote those reaching the observer in blue and green, respectively. The up-scattered photons reaching the observers from radially extended corona is shown in yellow, whereas photons reaching the observer from vertically elongated corona is shown in red. We show all other arrows in black.

6.3 Jet velocity: Role of Mass Accretion and Spin

We utilize the spectro-temporal properties of BH-XRBs under consideration to estimate their jet velocities. In doing so, we constrain the source spin and compute the disc radiative efficiency ($\eta_{\rm acc}$, Thorne 1974; Hobson et al. 2006), while obtaining the jet velocity (β) as a function of ε. The details of the estimated β and ε for different observations across all sources are provided in Table 3.

We observe that β generally increases with ε (see Fig. 10) and the estimated β values (see Table 3) are in good agreement with previously reported values measured from the proper motion of jet ejecta in different sources (Corbel et al. 2005; Miller-Jones et al. 2011; Miller-Jones et al. 2012; Hannikainen et al. 2009). We notice that in harder states (LHS and HIMS), jet velocity is sub-relativistic ($\lesssim 0.3\,c$) in nature, while in SIMS, it appears to be moderately relativistic ($\gtrsim 0.3 - 0.8\,c$) in presence of enhanced X-ray and radio luminosities, and sub-relativistic ($\lesssim 0.3\,c$) when luminosities

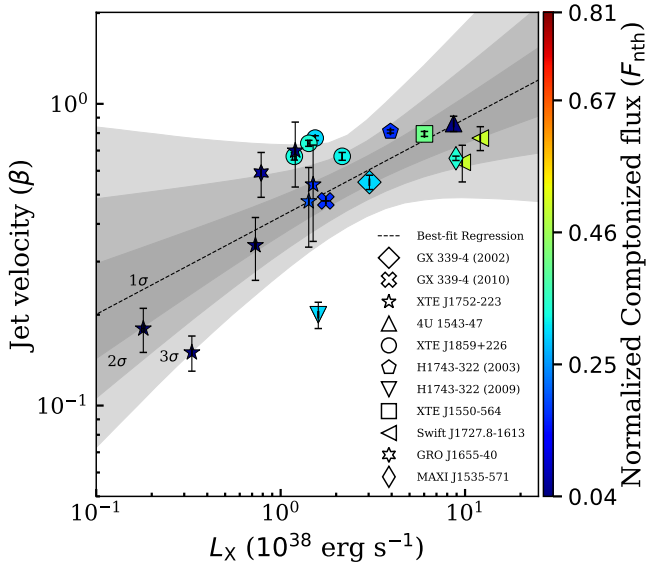

Figure 13. Correlation between X-ray luminosity and jet velocity. The dashed line represents the best-fit regression, while the shaded regions indicate the 1σ, 2σ and 3σ confidence intervals. The color bar encodes values of $F_{\rm nth}$. Individual sources under consideration are marked using different symbols. See the text for details.

are low. Furthermore, the correlation between intrinsic radio and X-ray luminosities (see Fig. 11), indicating that higher mass accretion rates lead to more powerful jets. This possibly indicates a weak dependence between jet velocity and black hole spin, while showing a much stronger correlation with accretion rates, in line with earlier studies (Fender et al. 2010; Russell et al. 2013; Fender & Gallo 2014; Aktar et al. 2015).

Furthermore, we investigate the relationship between jet velocity (β) and bolometric X-ray luminosity ($L_{\rm X}$) during SIMS, where $L_{\rm X}$ is generally higher than in HIMS. Following the approach of (Curran 2014), we generate 10^6 synthetic datasets using a bootstrap Monte Carlo method. Each dataset is constructed by sampling with replacement from the original β and $L_{\rm X}$ values. To incorporate measurement uncertainties, each sampled point is perturbed using a normal distribution centered on the sampled value with a standard deviation equal to its observational error. The obtained results are presented in Fig. 13, where the best fitted dashed line corresponds to $\log\beta = (0.33\pm0.11)\log L_{\rm X} - (0.37\pm0.06)$. Different symbols represent individual sources, and the color bar denotes the corresponding $F_{\rm nth}$ values. Shaded regions indicate the 1σ, 2σ, and 3σ confidence intervals, with increasing transparency. The Pearson correlation coefficient ~ 0.52 indicates a moderate positive correlation, suggesting that higher X-ray luminosity (equivalently mass accretion rate) is associated with faster jet velocities (β) during SIMS.

Finally, we mention that the present formalism bears limitations. The Doppler correction is expected to depend on both inclination (i) and jet velocity (β). Moreover, the assumption that the changes in normalized Comptonized flux during radio flaring events directly correspond to ε may be overly simplistic, as these flux variations could also reflect intrinsic changes in the accretion rate, rather than solely the outflow. Despite of all these, we argue that the basic conclusions of this work are expected to remain qualitatively unchanged.

We summarize the key findings of the present study in the context of disc-jet connection in BH-XRBs below:

(i) Strong Comptonized emissions with a radially extended corona appear to exhibit type-C QPOs in the BH-XRBs under consideration. Type-C QPOs show positive time lags for low-inclination sources, while negative time lags are observed for high-inclination sources, with the exception of Swift J1727.8−1613, XTE J1550−564, GRO J1655−40 and H1743−322 (2003 outburst).

(ii) Generally, type-A QPOs exhibit negative time lags with minimal Comptonized emissions regardless of source inclination angles. Our results indicate that type-A QPOs precede radio flares in several black hole X-ray binaries, including XTE J1752 − 223, XTE J1859 + 226, H1743 − 322, XTE J1550 − 564, and MAXI J1535 − 571. While this association points to a possible connection between type-A QPOs and jet ejection events, their infrequent detection calls for further observations to establish a robust relationship.

(iii) Type-B QPOs are typically observed in the SIMS or during the spectral state transition from HIMS to SIMS with weak Comptonized emissions similar to type-A QPOs. We observed that type-B QPOs are strongly associated with radio flares and exhibit positive lag for low inclination sources and both positive and negative lags for high inclination sources. This strongly suggests that type-B QPOs are linked to the geometry of a vertically extended corona.

(iv) Our findings demonstrate a strong correlation between the observed radio and X-ray luminosities, providing compelling evidence that jets are predominantly powered by accretion. We observe that during SIMS, the jet velocity appears to be moderately relativistic ($\gtrsim 0.3-0.8\,c$) when both X-ray and radio luminosities are high, and remains subrelativistic ($\lesssim 0.3\,c$) when the luminosities are low for the BH-XRBs under consideration.

7 ACKNOWLEDGMENT

Authors thank the reviewer for detailed and constructive comments, which help to improve the quality of the manuscript. SDC and SD thank the Department of Physics, IIT Guwahati, for providing the facilities to complete this work. SDC also acknowledges the financial support provided by Prime Minister Research Fellowship program to carry out this work. BGR thanks Gifu University, Japan for support. AN thanks GH, SAG; DD, PDMSA, and Director, URSC for encouragement and continuous support to carry out this research. This research has made use of data obtained from High Energy Astrophysics Archive Research Center (HEASARC) online services, provided by NASA/Goddard Space Flight Center.

8 DATA AVAILABILITY

The data utilized in this work is available in the websites of https://heasarc.gsfc.nasa.gov/cgi-bin/W3Browse/w3browse.pl and https://archive.hxmt.cn/proposal for *RXTE* and *HXMT*, respectively.

REFERENCES

Abdulghani Y., Lohfink A. M., Chauhan J., 2024, MNRAS, 530, 424
Agrawal P. C., 2017, Journal of Astrophysics and Astronomy, 38, 27
Agrawal P. C., et al., 2017, Journal of Astrophysics and Astronomy, 38, 30
Aktar R., Das S., Nandi A., 2015, MNRAS, 453, 3414
Aktar R., Das S., Nandi A., Sreehari H., 2017, MNRAS, 471, 4806
Aktar R., Nandi A., Das S., 2019, Ap&SS, 364, 22
Aneesha U., Mandal S., Sreehari H., 2019, MNRAS, 486, 2705
Aneesha U., Das S., Katoch T. B., Nandi A., 2024, MNRAS, 532, 4486
Antia H. M., et al., 2017, ApJS, 231, 10
Baby B. E., Agrawal V. K., Ramadevi M. C., Katoch T., Antia H. M., Mandal S., Nandi A., 2020, Monthly Notices of the Royal Astronomical Society, 497, 1197
Banerjee S., et al., 2024, ApJ, 964, 189
Bardeen J. M., Press W. H., Teukolsky S. A., 1972, ApJ, 178, 347
Belloni T., 2004, Nuclear Physics B Proceedings Supplements, 132, 337
Belloni T., Hasinger G., 1990, A&A, 230, 103
Belloni T., Homan J., Casella P., van der Klis M., Nespoli E., Lewin W. H. G., Miller J. M., Méndez M., 2005, A&A, 440, 207
Belloni T. M., Motta S. E., Muñoz-Darias T., 2011, Bulletin of the Astronomical Society of India, 39, 409
Belloni T. M., Zhang L., Kylafis N. D., Reig P., Altamirano D., 2020, MNRAS, 496, 4366
Bhuvana G. R., Radhika D., Agrawal V. K., Mandal S., Nandi A., 2021, MNRAS, 501, 5457
Bhuvana G. R., Aneesha U., Radhika D., Agrawal V. K., Mandal S., Katoch T., Nandi A., 2023, MNRAS, 520, 5828
Blandford R. D., Znajek R. L., 1977, MNRAS, 179, 433
Bogensberger D., et al., 2020, A&A, 641, A101
Bright J. S., et al., 2020, Nature Astronomy, 4, 697
Brocksopp C., et al., 2002, MNRAS, 331, 765
Brocksopp C., Miller-Jones J. C. A., Fender R. P., Stappers B. W., 2007, MNRAS, 378, 1111
Brocksopp C., Corbel S., Tzioumis A., Broderick J. W., Rodriguez J., Yang J., Fender R. P., Paragi Z., 2013, Monthly Notices of the Royal Astronomical Society, 432, 931
Cao X., et al., 2020, Science China Physics, Mechanics, and Astronomy, 63, 249504
Carotenuto F., et al., 2021, MNRAS, 504, 444
Casella P., Belloni T., Homan J., Stella L., 2004, A&A, 426, 587
Casella P., Belloni T., Stella L., 2005, ApJ, 629, 403
Chakrabarti S. K., 1999, A&A, 351, 185
Chakrabarti S., Titarchuk L. G., 1995, ApJ, 455, 623
Chatterjee A., Chakrabarti S. K., Ghosh H., 2017, MNRAS, 465, 3902
Chatterjee A., Dutta B. G., Nandi P., Chakrabarti S. K., 2020, MNRAS, 497, 4222
Chattopadhyay I., 2005, MNRAS, 356, 145
Chauhan J., et al., 2019, MNRAS, 488, L129
Chen J., Wang W., 2024, MNRAS, 527, 238
Chen W., Shrader C. R., Livio M., 1997, ApJ, 491, 312
Chen Y., et al., 2020, Science China Physics, Mechanics, and Astronomy, 63, 249505
Corbel S., Nowak M. A., Fender R. P., Tzioumis A. K., Markoff S., 2003, A&A, 400, 1007
Corbel S., Fender R. P., Tomsick J. A., Tzioumis A. K., Tingay S., 2004, ApJ, 617, 1272
Corbel S., Kaaret P., Fender R. P., Tzioumis A. K., Tomsick J. A., Orosz J. A., 2005, ApJ, 632, 504
Corbel S., Coriat M., Brocksopp C., Tzioumis A. K., Fender R. P., Tomsick J. A., Buxton M. M., Bailyn C. D., 2013, MNRAS, 428, 2500
Corral-Santana J. M., Casares J., Shahbaz T., Zurita C., Martínez-Pais I. G., Rodríguez-Gil P., 2013, in Revista Mexicana de Astronomia y Astrofisica Conference Series. pp 3–4
Corral-Santana J. M., Casares J., Muñoz-Darias T., Bauer F. E., Martínez-Pais I. G., Russell D. M., 2016, A&A, 587, A61
Curran P. A., 2014, arXiv e-prints, p. arXiv:1411.3816
Das S., Chattopadhyay I., Nandi A., Chakrabarti S. K., 2001, A&A, 379, 683
Das S., Nandi A., Stalin C. S., Rakshit S., Dihingia I. K., Singh S., Aktar R., Mitra S., 2022, MNRAS, 514, 1940
Davis S. W., El-Abd S., 2019, ApJ, 874, 23
Davis S. W., Blaes O. M., Hubeny I., Turner N. J., 2005, ApJ, 621, 372
Debnath D., Chatterjee K., Chatterjee D., Jana A., Chakrabarti S. K., 2021, MNRAS, 504, 4242
Dhawan V., Mirabel I. F., Rodríguez L. F., 2000, ApJ, 543, 373
Done C., Gierliński M., Kubota A., 2007, A&ARv, 15, 1
Dong Y., García J. A., Steiner J. F., Gou L., 2020, Monthly Notices of the Royal Astronomical Society, 493, 4409
Draghis P. A., Miller J. M., Costantini E., Gallo L. C., Reynolds M., Tomsick J. A., Zoghbi A., 2024, ApJ, 969, 40
Dutta B. G., Chakrabarti S. K., 2016, ApJ, 828, 101
Ebisawa K., et al., 1994, PASJ, 46, 375
Espinasse M., et al., 2020, ApJ, 895, L31
Fender R., 2001a, Astrophysics and Space Science Supplement, 276, 69
Fender R. P., 2001b, MNRAS, 322, 31
Fender R., Gallo E., 2014, Space Sci. Rev., 183, 323
Fender R. P., Garrington S. T., McKay D. J., Muxlow T. W. B., Pooley G. G., Spencer R. E., Stirling A. M., Waltman E. B., 1999, Astrophysical Letters and Communications, 38, 229
Fender R. P., Belloni T. M., Gallo E., 2004, MNRAS, 355, 1105
Fender R. P., Homan J., Belloni T. M., 2009, MNRAS, 396, 1370
Fender R. P., Gallo E., Russell D., 2010, MNRAS, 406, 1425
Fürst F., et al., 2015, ApJ, 808, 122
Gallo E., Fender R. P., Pooley G. G., 2003, in Durouchoux P., Fuchs Y., Rodriguez J., eds, New Views on Microquasars. p. 209 (`arXiv:astro-ph/0207551`), doi:10.48550/arXiv.astro-ph/0207551
Gandhi P., Rao A., Johnson M. A. C., Paice J. A., Maccarone T. J., 2019, MNRAS, 485, 2642
Gao H. Q., et al., 2014, MNRAS, 438, 341
García F., Méndez M., Karpouzas K., Belloni T., Zhang L., Altamirano D., 2021, MNRAS, 501, 3173
García J. A., et al., 2018, The Astrophysical Journal, 864, 25
Grebenev S. A., Mereminskiy I. A., Prosvetov A. V., Ducci L., Bozzo E., Savchenko V., Ferrigno C., 2018, The Astronomer's Telegram, 11306, 1
Greene J., Bailyn C. D., Orosz J. A., 2001, ApJ, 554, 1290
Hannikainen D., Campbell-Wilson D., Hunstead R., McIntyre V., Lovell J., Reynolds J., Tzioumis T., Wu K., 2001, Astrophysics and Space Science Supplement, 276, 45
Hannikainen D. C., et al., 2009, MNRAS, 397, 569
Harikrishna S., Sriram K., 2022, MNRAS, 516, 5148
Heida M., Jonker P. G., Torres M. A. P., Chiavassa A., 2017, ApJ, 846, 132
Hjellming R. M., Rupen M. P., 1995, Nature, 375, 464
Hobson M. P., Efstathiou G. P., Lasenby A. N., 2006, The Kerr geometry. Cambridge University Press, p. 310–354
Homan J., Belloni T., 2005, Ap&SS, 300, 107
Homan J., Wijnands R., van der Klis M., Belloni T., van Paradijs J., Klein-Wolt M., Fender R., Méndez M., 2001, ApJS, 132, 377
Homan J., Wijnands R., Kong A., Miller J. M., Rossi S., Belloni T., Lewin W. H. G., 2006, Monthly Notices of the Royal Astronomical Society, 366, 235
Homan J., et al., 2020, ApJ, 891, L29

Huppenkothen D., et al., 2019, ApJ, 881, 39
Hynes R. I., Haswell C. A., Chaty S., Shrader C. R., Cui W., 2002, MNRAS, 331, 169
Ingram A., Done C., Fragile P. C., 2009, MNRAS, 397, L101
Islam N., Zdziarski A. A., 2018, MNRAS, 481, 4513
Iyer N., Nandi A., Mandal S., 2015, ApJ, 807, 108
Jonker P. G., Nelemans G., 2004, MNRAS, 354, 355
Jonker P. G., et al., 2010, MNRAS, 401, 1255
Joshi R. K., Debnath S., Chattopadhyay I., 2022, ApJ, 933, 75
Kalemci E., Tomsick J. A., Buxton M. M., Rothschild R. E., Pottschmidt K., Corbel S., Brocksopp C., Kaaret P., 2005, ApJ, 622, 508
Karpouzas K., Méndez M., Ribeiro E. M., Altamirano D., Blaes O., García F., 2020, MNRAS, 492, 1399
Kumar R., Chattopadhyay I., 2013, MNRAS, 430, 386
Kuulkers E., et al., 2000, A&A, 358, 993
Kylafis N. D., Reig P., Papadakis I., 2020, A&A, 640, L16
Kylafis N. D., Reig P., Tsouros A., 2023, A&A, 679, A81
Liu C., et al., 2020, Science China Physics, Mechanics, and Astronomy, 63, 249503
Liu H. X., et al., 2022, ApJ, 938, 108
Longair M. S., 2011, High Energy Astrophysics
Ma R., Méndez M., García F., Sai N., Zhang L., Zhang Y., 2023, MNRAS, 525, 854
Ma R., et al., 2024, MNRAS, 528, 3864
Maccarone T. J., Coppi P. S., 2003, MNRAS, 338, 189
Majumder P., Dutta B. G., Nandi A., 2024, MNRAS, 527, 4739
Makishima K., Maejima Y., Mitsuda K., Bradt H. V., Remillard R. A., Tuohy I. R., Hoshi R., Nakagawa M., 1986, ApJ, 308, 635
Mandal S., Chakrabarti S. K., 2005, A&A, 434, 839
Markwardt C. B., Swank J. H., 2005, The Astronomer's Telegram, 414, 1
Markwardt C. B., et al., 2009, The Astronomer's Telegram, 2258, 1
Mata Sanchez D., Torres M. A. P., Casares J., Munoz-Darias T., Armas Padilla M., Yanes-Rizo I. V., 2024, arXiv e-prints, p. arXiv:2408.13310
McClintock J. E., Shafee R., Narayan R., Remillard R. A., Davis S. W., Li L.-X., 2006, ApJ, 652, 518
McClintock J. E., Remillard R. A., Rupen M. P., Torres M. A. P., Steeghs D., Levine A. M., Orosz J. A., 2009, ApJ, 698, 1398
McClintock J. E., Narayan R., Steiner J. F., 2014, Space Sci. Rev., 183, 295
Miller J. M., Remillard R. A., 2002, The Astronomer's Telegram, 98, 1
Miller-Jones J. C. A., Fender R. P., Nakar E., 2006, MNRAS, 367, 1432
Miller-Jones J. C. A., et al., 2009, The Astronomer's Telegram, 2062, 1
Miller-Jones J. C. A., Jonker P. G., Ratti E. M., Torres M. A. P., Brocksopp C., Yang J., Morrell N. I., 2011, Monthly Notices of the Royal Astronomical Society, 415, 306
Miller-Jones J. C. A., et al., 2012, MNRAS, 421, 468
Miller J. M., et al., 2018, ApJ, 860, L28
Mirabel I. F., Rodríguez L. F., 1994, Nature, 371, 46
Mirabel I. F., Rodríguez L. F., 1999, ARA&A, 37, 409
Mirabel I. F., Dhawan V., Chaty S., Rodriguez L. F., Marti J., Robinson C. R., Swank J., Geballe T., 1998, A&A, 330, L9
Miyamoto S., Kitamoto S., Mitsuda K., Dotani T., 1988, Nature, 336, 450
Molla A. A., Chakrabarti S. K., Debnath D., Mondal S., 2017, ApJ, 834, 88
Monageng I. M., Motta S. E., Fender R., Yu W., Woudt P. A., Tremou E., Miller-Jones J. C. A., van der Horst A. J., 2021, MNRAS, 501, 5776
Mondal S., 2009, The Astrophysical Journal, 708, 1442
Mondal S., Jithesh V., 2023, MNRAS, 522, 2065
Morgan E., Swank J., Markwardt C., Gehrels N., 2005, The Astronomer's Telegram, 550, 1
Motta S., Belloni T., Homan J., 2009, MNRAS, 400, 1603
Motta S., Muñoz-Darias T., Belloni T., 2010, MNRAS, 408, 1796
Motta S. E., Casella P., Henze M., Muñoz-Darias T., Sanna A., Fender R., Belloni T., 2015, MNRAS, 447, 2059
Motta S. E., Belloni T., Stella L., Pappas G., Casares J., Muñoz-Darias A. T., Torres M. A. P., Yanes-Rizo I. V., 2022, MNRAS, 517, 1469
Muñoz-Darias T., Motta S., Pawar D., Belloni T. M., Campana S., Bhattacharya D., 2010, MNRAS, 404, L94
Méndez M., Karpouzas K., García F., Zhang L., Zhang Y., Belloni T., Altamirano D., 2022, Nature Astronomy, 6
Nandi A., Manickam S. G., Rao A. R., Chakrabarti S. K., 2001, MNRAS, 324, 267
Nandi A., Debnath D., Mandal S., Chakrabarti S. K., 2012, A&A, 542, A56
Nandi A., et al., 2018, Ap&SS, 363, 90
Nandi A., Das S., Majumder S., Katoch T., Antia H. M., Shah P., 2024, MNRAS, 531, 1149
Narayan R., McClintock J. E., 2013, arXiv e-prints, p. arXiv:1312.6698
Negoro H., et al., 2017, The Astronomer's Telegram, 10699, 1
Negoro H., et al., 2023, The Astronomer's Telegram, 16205, 1
Neustroev V. V., Veledina A., Poutanen J., Zharikov S. V., Tsygankov S. S., Sjoberg G., Kajava J. J. E., 2014, MNRAS, 445, 2424
Nowak M. A., Vaughan B. A., Wilms J., Dove J. B., Begelman M. C., 1999, ApJ, 510, 874
Orosz J. A., Jain R. K., Bailyn C. D., McClintock J. E., Remillard R. A., 1998, ApJ, 499, 375
Orosz J. A., McClintock J. E., Remillard R. A., Corbel S., 2004, The Astrophysical Journal, 616, 376
Orosz J. A., Steiner J. F., McClintock J. E., Torres M. A. P., Remillard R. A., Bailyn C. D., Miller J. M., 2011, ApJ, 730, 75
Park S. Q., et al., 2004, ApJ, 610, 378
Parker M. L., et al., 2016, ApJ, 821, L6
Payne D. G., 1980, ApJ, 237, 951
Peirano V., Méndez M., García F., Belloni T., 2023, MNRAS, 519, 1336
Peng J.-Q., et al., 2024, ApJ, 960, L17
Peters W. M., Polisensky E., Clarke T. E., Giacintucci S., Kassim N. E., 2023, The Astronomer's Telegram, 16279, 1
Ponti G., Fender R. P., Begelman M. C., Dunn R. J. H., Neilsen J., Coriat M., 2012, MNRAS, 422, L11
Radhika D., Nandi A., 2014, Advances in Space Research, 54, 1678
Radhika D., Nandi A., Agrawal V. K., Seetha S., 2016, MNRAS, 460, 4403
Radhika D., Sreehari H., Nandi A., Iyer N., Mandal S., 2018, Ap&SS, 363, 189
Reig P., Belloni T., van der Klis M., Méndez M., Kylafis N. D., Ford E. C., 2000, ApJ, 541, 883
Remillard R., 2003, The Astronomer's Telegram, 138, 1
Remillard R. A., McClintock J. E., 2006, ARA&A, 44, 49
Remillard R. A., Sobczak G. J., Muno M. P., McClintock J. E., 2002, ApJ, 564, 962
Riemann B., 2004, Collected papers, german edn. Kendrick Press, Heber City, UT
Rodriguez J., Varnière P., 2011, ApJ, 735, 79
Russell D. M., Gallo E., Fender R. P., 2013, MNRAS, 431, 405
Russell T. D., et al., 2019, ApJ, 883, 198
Russell D. M., Casella P., Kalemci E., Vahdat Motlagh A., Saikia P., Pirbhoy S. F., Maitra D., 2020, Monthly Notices of the Royal Astronomical Society, 495, 182
Rutledge R., Fox D., Smith D. A., 1998, The Astronomer's Telegram, 37, 1

Rybicki G. B., Lightman A. P., 1979, Radiative processes in astrophysics
Shafee R., McClintock J. E., Narayan R., Remillard R. A., Davis S. W., Li L., 2006, in AAS/High Energy Astrophysics Division #9. p. 1.86
Shakura N. I., Sunyaev R. A., 1973, A&A, 24, 337
Shapiro S. L., Teukolsky S. A., 1983, Black holes, white dwarfs and neutron stars. The physics of compact objects. A Wiley-Interscience Publication, New York: Wiley, 1983, doi:10.1002/9783527617661
Shaposhnikov N., Swank J., Shrader C. R., Rupen M., Beckmann V., Markwardt C. B., Smith D. A., 2007, ApJ, 655, 434
Shaposhnikov N., Markwardt C., Swank J., Krimm H., 2010, The Astrophysical Journal, 723, 1817
Shaw A. W., Charles P. A., Casares J., Hernández Santisteban J. V., 2016, MNRAS, 463, 1314
Shidatsu M., et al., 2011, PASJ, 63, S785
Singh K. P., et al., 2017, Journal of Astrophysics and Astronomy, 38, 29
Slaný P., Stuchlík Z., 2008, A&A, 492, 319
Smith D. A., 1999, The Astronomer's Telegram, 47, 1
Smith D. A., Levine A., Wood A., 1998, The Astronomer's Telegram, 25, 1
Smith D. M., Belloni T., Heindl W. A., Kalemci E., Remillard R., Nowak M., Swank J. H., Corbel S., 2002, The Astronomer's Telegram, 95, 1
Sobczak G. J., McClintock J. E., Remillard R. A., Levine A. M., Morgan E. H., Bailyn C. D., Orosz J. A., 1999, ApJ, 517, L121
Soldi S., Miller J., Kuulkers E., Caballero-Garcia M. D., Diaz Trigo M., 2007, The Astronomer's Telegram, 986, 1
Soleri P., et al., 2010, MNRAS, 406, 1471
Sreehari H., Nandi A., 2021, MNRAS, 502, 1334
Sreehari H., Nandi A., Radhika D., Iyer N., Mandal S., 2018, Journal of Astrophysics and Astronomy, 39
Sreehari H., Ravishankar B. T., Iyer N., Agrawal V. K., Katoch T. B., Mandal S., Nandi A., 2019, MNRAS, 487, 928
Sridhar N., Bhattacharyya S., Chandra S., Antia H. M., 2019, MNRAS, 487, 4221
Sriram K., Harikrishna S., Choi C. S., 2021, ApJ, 911, 127
Steiner J. F., Narayan R., McClintock J. E., Ebisawa K., 2009, PASP, 121, 1279
Steiner J. F., et al., 2011, Monthly Notices of the Royal Astronomical Society, 416, 941
Steiner J. F., McClintock J. E., Reid M. J., 2012, ApJ, 745, L7
Stevens A. L., Uttley P., 2016, Monthly Notices of the Royal Astronomical Society, 460, 2796
Tanaka Y., Shibazaki N., 1996, ARA&A, 34, 607
Tetarenko B. E., Sivakoff G. R., Heinke C. O., Gladstone J. C., 2016, The Astrophysical Journal Supplement Series, 222, 15
Thorne K. S., 1974, ApJ, 191, 507
Titarchuk L., Fiorito R., 2004, ApJ, 612, 988
Tomsick J. A., Kaaret P., 2000, ApJ, 537, 448
Tomsick J. A., Kalemci E., Corbel S., Kaaret P., 2002, IAU Circ., 7837, 3
Uttley P., Cackett E. M., Fabian A. C., Kara E., Wilkins D. R., 2014, A&ARv, 22, 72
Vadawale S. V., Rao A. R., Chakrabarti S. K., 2001, A&A, 372, 793
Varnière P., Tagger M., Rodriguez J., 2012, A&A, 545, A40
Wijnands R., Homan J., van der Klis M., 1999, ApJ, 526, L33
Wilms J., Allen A., McCray R., 2000, ApJ, 542, 914
Wood C. M., et al., 2021, MNRAS, 505, 3393
Wood C. M., et al., 2024, arXiv e-prints, p. arXiv:2405.12370
Xu Y., et al., 2018, ApJ, 865, 18
Yadav J. S., et al., 2016, in den Herder J.-W. A., Takahashi T., Bautz M., eds, Society of Photo-Optical Instrumentation Engineers (SPIE) Conference Series Vol. 9905, Space Telescopes and Instrumentation 2016: Ultraviolet to Gamma Ray. p. 99051D, doi:10.1117/12.2231857
Yamaoka K., et al., 2010, The Astronomer's Telegram, 2380, 1
Yamaoka K., et al., 2012, PASJ, 64, 32
Yanes-Rizo I. V., et al., 2022, MNRAS, 517, 1476
Yang Z.-X., et al., 2024, ApJ, 970, L33
Yu W., et al., 2024, MNRAS, 529, 4624
Zdziarski A. A., Johnson W. N., Magdziarz P., 1996, MNRAS, 283, 193
Zdziarski A. A., Ziółkowski J., Mikołajewska J., 2019, MNRAS, 488, 1026
Zdziarski A. A., Szanecki M., Poutanen J., Gierliński M., Biernacki P., 2020, MNRAS, 492, 5234
Zhang S., Lu F. J., Zhang S. N., Li T. P., 2014, in Takahashi T., den Herder J.-W. A., Bautz M., eds, Society of Photo-Optical Instrumentation Engineers (SPIE) Conference Series Vol. 9144, Space Telescopes and Instrumentation 2014: Ultraviolet to Gamma Ray. p. 914421, doi:10.1117/12.2054144
Zhang Y., et al., 2023, MNRAS, 520, 5144
Zurita C., et al., 2002, MNRAS, 334, 999
van den Eijnden J., Ingram A., Uttley P., Motta S. E., Belloni T. M., Gardenier D. W., 2017, MNRAS, 464, 2643
van der Klis M., 1988, in Ögelman H., van den Heuvel E. P. J., eds, NATO Advanced Science Institutes (ASI) Series C Vol. 262, NATO Advanced Science Institutes (ASI) Series C. Kluwer Academic Publishers, Dordrecht, p. 27